Thesis for the Degree of Doctoral Philosophy in The Natural Sciences

Time Resolved Diffraction Studies of Structural Changes in Sensory Rhodopsin

Robert Bosman

UNIVERSITY OF GOTHENBURG

Department of Chemistry and Molecular Biology

Gothenburg, 2019

Thesis for the Degree of Doctoral Philosophy in The Natural Sciences

Time Resolved Diffraction Studies of Structural Changes in Sensory Rhodopsin

Robert Bosman

Cover Photo: Light activated isomorphous difference density superimposed onto Sensory Rhodopsin II

ISBN 978-91-7833-736-1 (Print)
ISBN 978-91-7833-737-8 (PDF)
Available online at http://hdl.handle.net/2077/62253
Department of chemistry and molecular biology
Division of biochemistry and structural biology
University of Gothenburg
SE-405 30 Göteborg Sweden

Printed by BrandFactory
Göteborg , Sweden 2019

To Tyson and Vilda
For all the inquisitive looks

Abstract

Responding to different light conditions is an essential process for many organisms on earth. Unicellular organisms are no exception to this and mechanisms for controlling cellular movement must often be sensitive to light. Light sensing proteins commonly have internally bound chromophores that, when activated by specific light wavelengths, propagate structural changes through a protein to produce an appropriate cellular response. Microbial rhodopsins are a family of transmembrane proteins that harness light to perform a range of functions. These rhodopsins have been found to act as ion pumps, channels and light sensing proteins. They all utilize similar chemistry through a covalently bound retinal to perform these diverse functions. In this thesis, time-resolved structural techniques are utilized to track the changes in sensory rhodopsin II (SRII) a photophobic blue-light sensor in archaea that protects the cell against harmful UV-radiation. SRII is bound in the membrane to a transducer protein (HtrII) that extends into the cell to affect a response.

Time-resolved structural biology has undergone a period of rapid methodological development. Inspired by the data collection challenges presented by X-ray free electron lasers (XFELS), serial crystallography has proved remarkably effective in resolving protein dynamics in crystals by time-resolved studies. These methods have more recently been used at synchrotrons. Recent work has shown that time-resolved serial millisecond crystallography (TR-SMX) on membrane protein microcrystals growing in lipidic cubic phase (LCP) is possible at synchrotrons. This complements time-resolved X-ray solution scattering (TR-XSS) methods already employed at synchrotron sources to measure protein dynamics. In this thesis, we utilize both methods to gain new insight into SRII and SRII-HtrII dynamics and structure.

The papers presented here outline new crystallization conditions for SRII and SRII-HtrII that do not require lipid reconstitution. At the Swiss Light Source, we measured a light-activated structure for SRII that provides a

structural explanation of the long-lived signalling states using TR-SMX. We also collected a low-resolution room temperature SRII-HtrII structure that reveals new features and which paves the way for time-resolved serial femtosecond crystallography (TR-SFX) measurements at XFELs., Solution X-ray scattering experiments were carried out on SRII and SRII-HtrII to observe complex dynamics. These revealed that the presence of transducer inhibits the EF-helix motion, providing evidence that this motion in involved in signal transduction.

Sammanfattning på Svenska

Att kunna uppfatta och reagera på olika ljusförhållanden är viktigt för många organismer på jorden. Encelliga organismer är inget undantag och mekanismer för att kontrollera deras cellrörelser är ofta ljusakänsliga. Dessa protein har vanligtvis internt bundna kromoforer som, när de aktiveras av specifika våglängder av ljus, propagerar strukturella förändringar genom sin interna struktur för att ge en lämplig cellulär respons. En typ av ljusaktiverade proteiner är mikrobiella rhodopsiner, en familj av transmembranproteiner som utnyttjar ljus för att utföra en rad olika funktioner. Rhodopsiner har visat sig fungera som jonpumpar, jonkanaler och ljussensorer. Dessa funktioner utförs genom den kovalent bundna kromoforen Retinal, något som är gemensamt för alla rhodopsiner. I denna avhandling används flera tidsupplösta strukturbiologiska undersökningsmetoder för att förstå och spåra förändringarna i Sensory Rhodopsin II (SRII). SRII är en fotofob blåljussensor i archaea, vars funktion är att skydda cellen mot skadlig UV-strålning. SRII är lokaliserat i cellmembranet och är där bundet till ett transducer-protein (HtrII) som sträcker sig in i cellen där det i sin tur kan påverka vidare funktioner.

Metoder för att genomföra tidsupplöst strukturell biologi har genomgått en period av snabb utveckling. Inspirerat av de utmaningar inom datainsamling som presenterats av X-Ray Free-Electron Lasers (XFELs) har seriell kristallografi visat sig vara anmärkningsvärt effektivt för att genomföra tidsupplösta studier av proteindynamik i kristaller. Dessa metoder har nyligen börjat användas även vid synkrotroner. Tidsupplöst seriell millisekund-kristallografi (Time-Resolved Serial-Millisecond-Crystallography,TR-SMX) utförd på membranprotein-mikrokristaller som växt i lipidisk kubisk fas (Lipidic Cubic Phase, LCP) är möjlig vid synkrotroner. Detta komplementerar metoder för tidsupplöst röntgendiffraktion av proteiner i lösning (Time-Resolved X-Ray Solution Scattering, TR-XSS) som redan använts vid synkrotronkällor för att undersöka proteindynamik. I

denna avhandling har båda metoderna använts för att få ny förståelse för SRII och SRII-HtrIIs struktur och dynamik.

De vetenskapliga artiklar som presenteras här beskriver nya metoder för kristallisation av SRII och SRII-HtrII som inte kräver en insättning av proteinet i membranlipider. Vid den Schweiziska synkrotronen, Swiss Light Source, uppmättes en struktur av ljusaktiverat SRII som, med hjälp av TR-SMX, gav en strukturell förklaring till dess långlivade signaltillstånd. Vi har också mätt en lågupplöst struktur för SRII-HtrII i rumstemperatur som avslöjar nya funktioner och som banar vägen för att genomföra tidsupplösta seriella femtosekund-kristallografimätningar (Time-Resolved Serial-Femtosecond-Crystallography, TR-SFX) vid en XFEL. TR-XSS mätningar har gjorts på SRII och SRII-HtrII för att studera den komplexa dynamiken vid fotoaktivering. Dessa mätningar visade att transducer-proteinet hämmar rörelserna hos EF-helixarna vilket indikerar att denna rörelse är involverad i proteinets signalöverföringsdynamik.

Contribution list

Paper I I crystallised sensory rhodopsin II. I attended the experiment and collected data. I made contributions to the manuscript.

Paper II I attended the experiment and collected data.

Paper III I purified and crystallised sensory rhodopsin II. I attended the experiment and collected data. I analysed the data and performed the structural refinement. I prepared the manuscript.

Paper IV I purified and crystallised sensory rhodopsin II and transducer. I attended the experiment and collected data. I analysed the data and performed the structural refinement. I prepared the manuscript.

Paper V I purified sensory rhodopsin II and transducer. I attended the experiment and collected data. I helped analyse the data. I made contributions to the manuscript.

List of publications

Paper I Andersson, R., Safari, C., Bath, P., **Bosman, R.**, Shilova, A., Dahl, P., Ghosh, S., Dunge, A., Kjeldsen-Jensen, R., Nan, J., Shoeman, R. L., Kloos, M., Doak, R. B., Mueller, U., Neutze, R. & Branden, G . "Well-based Crystallization of Lipidic Cubic Phase Microcrystals for Serial X-ray Crystallography Experiments." Acta Crystallographica Section D 75, no. 10 (2019): 937-946.

Paper II Nogly, P., Weinert, T., James, D., Carbajo, S., Ozerov, D., Furrer, A., Gashi, D., Borin, V., Skopintsev, P., Jaeger, K., Nass, K., Båth, P., **Bosman, R.**, Koglin, J., Seaberg, M., Lane, T., Kekilli, D., Brünle, S., Tanaka, T., Wu, W., Milne, C., White, T., Barty, A., Weierstall, U., Panneels, V., Nango, E., Iwata, S., Hunter, M., Schapiro, I., Schertler, G., Neutze, R., Standfuss, J. "Retinal Isomerization in Bacteriorhodopsin Captured by a Femtosecond X-ray Laser." Science (New York, N.Y.) 361, no. 6398 (2018): 145-.

Paper III **Bosman, R.**, Ortolani, G., Ghosh, S., Björg Úlfarsdóttir, T., James, D., Börjesson, P., Hammarin, G., Weinert, T., Dworkowski, F., Takashi, T., Standfuss, J., Brändén, G., Neutze, R. “Structural explanation for the prolonged photocycle in Sensory Rhodopsin II revealed by room temperature serial millisecond crystallography.” Manuscript.

Paper IV **Bosman, R.**, Ortolani, G., Björg Úlfarsdóttir, T., Ghosh, S., James, D., Hammarin, G., Börjesson, P., Weinert, T., Dworkowski, F., Takashi, T., Standfuss, J., Brändén, G., Neutze, R. "Serial millisecond crystallography structure of the Sensory Rhodopsin II: transducer complex." Manuscript.

Paper V **Bosman, R.**, Sarabi, D., Ghosh, S., Ortolani, G., Reymer, A., Levantino, M., Nors Pedersen, M., Sander, M., Båth, P., Börjesson, P., Dods, R., Hammarin, G., Safari, C., Björg Úlfarsdóttir, T., Wulff, M., Brändén, G., Neutze, R. "Time resolved x-ray scattering observations of light induced structural changes in Sensory Rhodopsin II." Manuscript.

Related publications

Publications that I have co-authored but that are not included in this thesis:

Andersson, R., Safari, C., Dods, R., Nango, E., Tanaka, R., Yamashita, A., Nakane, T., Tono, K., Joti, Y., Båth, P., Dunevall, E., **Bosman, R.**, Nureki, O., Iwata, S., Neutze, R. & Brändén, G. "Serial Femtosecond Crystallography Structure of Cytochrome C Oxidase at Room Temperature." Sci Rep 7, no. 1 (2017): 4518.

Dods, R., Båth, P., Arnlund, D., Beyerlein, K.R., Nelson, G., Liang, M., Harimoorthy, R., Berntsen, P., Malmerberg, E., Johansson, L., Andersson, R., **Bosman, R.**, Carbajo, S., Claesson, E., Conrad, C.E., Dahl, P., Hammarin, G., Hunter, M.S., Li, C., Lisova, S., Milathianaki, D., Robinson, J., Safari, C., Sharma, A., Williams, G., Wickstrand, C., Yefanov, O., Davidsson, J., DePonte, D.P., Barty, A., Brändén, G., Neutze, R. "From Macrocrystals to Microcrystals: A Strategy for Membrane Protein Serial Crystallography." Structure 25, no. 9 (2017): 1461-468.e2.

Claesson, E., Yuan Wahlgren, W., Takala, H., Pandey S., Castillon, L., Kuznetsova, V., Henry, L., Carrillo, M., Panman, M., Kübel, J., Nanekar, R., Isaksson, L., Nimmrich, A., Cellini, A., Morozov, D., Maj, M., Kurttila, M., **Bosman, R.**, Nango, E., Tanaka, R., Tanaka, T., Fangjia, L., Iwata, S., Owada, S., Moffat, K., Groenhof, G., Stojković, E.A., Ihalainen, J.A., Schmidt, M., Westenhoff, S. "The primary structural photoresponse of phytochrome proteins captured by a femtosecond X-ray laser. " bioRxiv 789305; doi: https://doi.org/10.1101/789305

Abbreviations

SRII	sensory rhodopsin II
HtrII	transducer protein
XFEL	X-ray free electron laser
(TR)-SMX	(time-resolved) serial millisecond crystallography
LCP	lipidic cubic phase
TR-XSS	time-resolved solution scattering
bR	bacteriorhodopsin
ATP	adenosine triphosphate
TM	transmembrane
LGIC	ligand gated ion channel
GPCRs	G-protein coupled receptors
VGICs	voltage gated ion channels
RTKs	receptor tyrosine kinases
ASR	anabaena sensory rhodopsin
hR	Halorhodopsin
Ch2	channelrhodopsin-2
Asp	asparagine
Thr	threonine
Arg	arginine
Glu	glutamic acid
Tyr	tyrosine
Ala	alanine
Cys	cystine
Ser	serine
SRI	sensory rhodopsin I
FTIR	Fourier-transform infrared spectroscopy

TRX	time-resolved X-ray crystallography
(TR-)WAXS	(time-resolved) wide-angle X-ray scattering
(TR-)SAXS	(time-resolved) side-angle X-ray scattering
(TR-)cryo-EM	(time-resolved) cryo-electron microscopy
GDP	guanosine-diphosphate
GTP	guanosine-triphosphate
IPTG	isopropyl-β-D-thiogalactopyranoside

Contents

1. Introduction 1
1.1 Signalling across the membrane 2
1.1.1 Different transmembrane signals, many and varied 4
1.2 Microbial rhodopsins 6
1.2.1 Bacteriorhodopsin 9
1.2.2 Sensory rhodopsin II and transducer 10
1.4 Scope of the thesis 14
2. Membrane protein crystallography 17
2.1 Purification of membrane proteins 17
2.1.1 Protein expression 18
2.1.2 Solubilisation 19
2.1.3 Chromatography 19
2.2 Crystallization 21
2.2.1 What are crystals? 21
2.2.2 Crystal growth 22
2.2.4 Lipidic cubic phase 24
2.3 Paper I: Well-based crystallization for serial crystallography 25
2.3.1 New SRII crystals 25
2.3.2 Well-based crystallization general methodology 26
2.3.3 Well-based crystallization advantages 26
2.3.4 SRII at large scale 27
2.3.5 Paper I – summary 28
3. X-ray scattering, theory and practice 31
3.1 General scattering theory 31
3.2 Crystallographic diffraction 34
3.2.1 X-ray crystallography data analysis 37

3.2.2 Crystallographic refinement 38
3.2.3 Conventional cryo-crystallography 38
3.2.4 Serial crystallography – new rules 39
3.3 Time-resolved structural biology 40
3.3.1 Time-resolved X-ray crystallography; lights, camera, action 40
3.3.2 Time-resolved millisecond serial crystallography with LCP jets 43
3.3 Solution scattering 44
3.3.1 Solution scattering theory 45
3.3.2 Time-resolved wide-angle X-ray scattering; lights, contrast, action 47
3.3.3 Difference scattering 48
4. Sensory rhodopsin II and bacteriorhodopsin 51
4.1 Paper II: Ultrafast study of retinal isomerization in bacteriorhodopsin 51
4.1.1 Ultrafast measurements 51
4.1.2 Ultrafast retinal isomerization 52
4.1.3 Immediate water disordering 53
4.1.4 Implications for SRII 54
4.2 Paper III: SRII, time-resolved millisecond crystallography 54
4.2.1 Data collection and handling 54
4.2.2 Overall map comparison 56
4.2.3 Hydrogen bond coordination on Helix-G 57
4.2.4 Disorder waters and proton gating 58
4.2.5 Mechanics 59
5. SRII and transducer 61
5.1 Paper IV: serial structure of SRII-HtrII 61
5.1.1 Crystallizing the complex, archaeal lipids 61
5.1.2 Serial crystallography 63
5.1.3 The serial structure density 64

5.1.4 Extra helical density 65
5.1.5 Paper IV: conclusion 66
5.2 Paper V: SRII-HtrII signalling via TR-XSS 67
5.2.1 – Data collection 67
5.2.2 Experimental difference curves 68
5.2.3 Data analysis and modelling 69
5.2.4 Discussion 71
6. Conclusions and future perspectives 73
6.1 Conclusions 73
6.2 Future perspectives 74
8. Acknowledgements 75
9. Bibliography 78

1. Introduction

A protein's primary sequence is a marvel of evolutionary encoding [1]. For any given protein a stable secondary and tertiary structure, along with folding pathway considerations are all encoded into the primary sequence[2]. Studying protein homologs has proved an effective method to discern how proteins sequences are adapted to carry out the same chemistry in varying conditions[3]. Conversely, studying similarly structured proteins but with varying functions allows us to understand the underlying structure-function relationship. This layer of encoding in the protein sequence governs the distinct motions required for protein function. Therefore, functional movements are the product of both the dynamic regimes allowed by differing protein sequences and specific interactions induced after protein activation, e.g. binding, isomerization or polarisation.

This presents a complex picture of general protein dynamic modes juxtaposed against more specific functionally relevant movements. New tools in structural biology allow protein changes to be tracked at distinct time points with high spatial accuracy after activation. Following a proteins reaction coordinates this way highlights the relative importance of different amino acids and protein regions to function. Careful comparison with structural or functional homologs allows a better understanding to the structure-function relationship.

This thesis focuses on sensory rhodopsin II (SRII) and its cognate transducer (HtrII). We compare our results with recent results in bacteriorhodopsin (bR), a structural homolog. SRII is a photophobic receptor for near-UV blue light, while bR is a proton pump used to produce a proton gradient for adenosine triphosphate (ATP) production [4]. Both proteins are found in archaea and share almost identical tertiary structure. However, their function and activation time varies significantly. This affords two opportunities; to study the structural differences between identically structured but differently functioning proteins and to investigate how the general microbial rhodopsin frame is adapted for signal transduction in SRII.

1.1 Signalling across the membrane

To avoid harmful environments, cellular organisms have developed various feedback mechanisms. Ask anyone who has flinched away from a blinding light. As the membrane is an entropically formed physical definition for the cell, altering the cell's chemistry requires an energetically favourable signal transmission across the membrane. These processes typically require converting external signals into structural changes within a receptor protein that propagates into the cell. Furthermore, these signals must be distinct and fast enough to generate an accurate and appropriate cellular response.

Cell membranes (Fig 1.1) are comprised of lipid molecules, predominantly phospholipids. All biological lipids are amphipathic, in that have polar (hydrophilic) head groups and non-polar (hydrophobic) tails. In water, lipid molecules attempt to 'bury' their non-polar tails by packing them next to other tails to achieve an entropically favourable configuration. A bilayer is a particular ordering where two lipid layers back onto one another with their non-polar tails in the core (Fig 1.1). While cell membranes are far more intricate then this simple model suggests[5,6], it is a convenient basic model.

The lipid bilayer that outlines the cell is the cell membrane (Fig 1.1). A key problem thus arises when considering how a molecule can traverse both the polar and non-polar membrane regions. How does the myriad of external signals, small molecules, proteins, light, electrical or mechanic forces that define the cells external environment interact with this barrier and elicit an appropriate cellular response? Membrane proteins utilize the subtle biochemistry afforded to the amino acid code to manage this communication. The proteins take three primary forms: lipid anchored, peripheral and transmembrane (Fig 1.1). Lipid anchored proteins are covalently linked to a lipid in the membrane. Peripheral membrane proteins

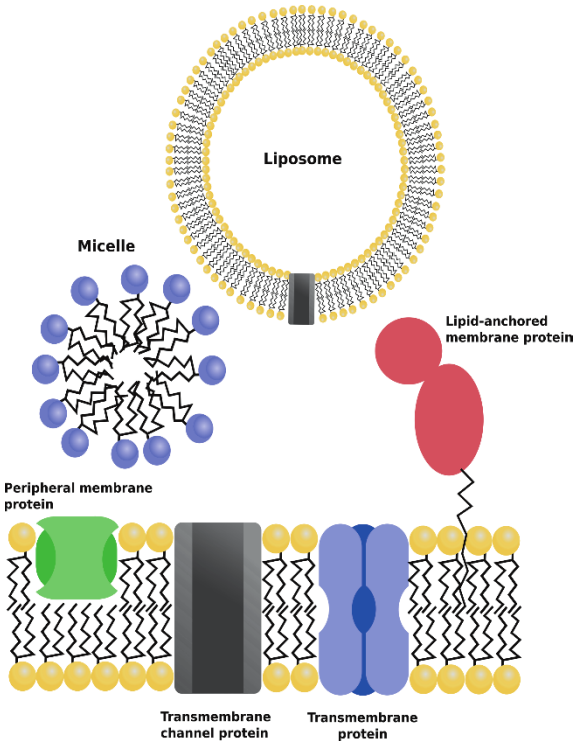

Figure 1.1, Overview of basic detergent and lipid structures. Liposomes are circular bilayer structures that can be used for assays or as a structure to reconstitute membrane proteins into before crystallization. Micelles are made from detergents rather than a bilayer. The tails of the lipids are buried at the center of the ball. Given its hydrophobic core, proteins can place their transmembrane region within it as protection from water.

are located in the membrane but do not traverse the membrane. Transmembrane (TM) proteins sit within the membrane itself, accessing both membrane sides. To deal with the bilayer's non-polar and polar nature, these proteins contain a hydrophobic core with hydrophilic cytoplasmic and extracellular regions. As only TM proteins access both sides of the bilayer, membrane receptors are normally TM proteins. When activated, they transmit a signal across the membrane.

1.1.1 Different transmembrane signals, many and varied

While this thesis focuses on light sensing proteins, I will take a brief moment to discuss different signals and proteins for transmembrane signalling with greater focus on ligand-receptor interactions (Fig 1.2). Signalling transmembrane proteins typically respond to either mechanical, chemical or electrical signals. Mechanosensors trigger cellular responses to external pressure or strain on the cell[7]. Mechanosensors are associated with cell adhesion, for example integrins required for multi-cellular interactions in eukaryotes, but they are also found in yeast[8]. In contrast, other types of mechanosensors are found in prokaryotes. These respond to osmotic pressure or contain integrins and are involved in biofilm development[9]. Electrical signals in biology are primarily electrical potentials generated across membranes. Voltage gated ion channels (VGICs) are the dominant super-family of electrical signalling transmembrane proteins, they work both through sensing via specific sensor domains and also responding to changes in membrane potentials[10]. As the sensor domain is activated, it triggers pore formation between several sub-units and the opening of a specific ion pore. Interestingly, growing evidence suggests that these ion sensors may also activate other signalling mechanisms such as kinase pathways to effect a response[11].

Arguably, the most well studied transmembrane signal transmission mechanisms are receptor-ligand systems. Ligands can be hormones, neurotransmitters, external signals (e.g. tastants), or indeed other transmembrane receptors. While it is difficult to subdivide the myriad of receptors, there are several large super-families to note: ligand gated ion channels (LGIC)[17], receptor tyrosine kinases and G-protein coupled receptors (GPCRs). Like the VGICs, LGICs are primarily multimeric pore forming channels that transport ions. These groups differ as LGICs bind small molecules rather than responding to membrane potentials like VGICs. LGICs can be classified in three distinct groups[18]: the cys-loop receptors[17], ionotropic glutamate receptors and ATP-gated channels. Cys-looped

receptors, so named after conserved cysteine residues which are important for function, they are highly represented as neurotransmitters[19,20,21].

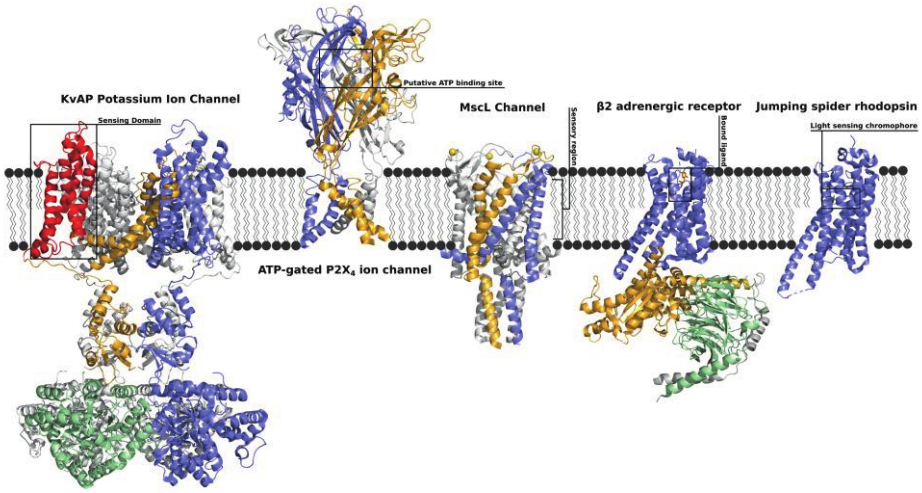

Figure 1.2, Structures for different signaling membrane proteins, The voltage gated ion channel (VGIC) KvAP, with a membrane sensing domain (2r9r)[12]. ATP-gated $P2X_4$ ion channels, with putative binding sight highlighted (3I5D)[13]. Mechanosensing channel responds to membrane distortions through its transmembrane domain (2OAR)[14]. Ligand binding β-adrenergic receptor bound to the G-protein complex (3SN6)[15]. Jumping spider rhodopsin a meta-stable opsin and light driven G-protein coupled receptor (6I9K)[16]

The ionotropic glutamate receptors bind to neurotransmitter derivatives of glutamate, they are typically tetramers with 2-fold symmetry[22]. Finally, ATP-gated channel receptor (PX2 receptor) binds extracellular ATP and form cationic pores through the membrane and are widely expressed throughout the human body[23,24].

Receptor tyrosine kinases (RTKs) are a family of transmembrane receptors that play a predominate role in hormone signalling. RTK activation

is achieved through dimerization of the receptors. This can be mediated by the ligand, the receptor or by a combination of both. RTKs are the focus of intense research, since their prevalence as growth factor receptors means that naturally occurring mutations are causal to several cancers[25].

In even a brief tour of ligand receptors, the GPCRs cannot be ignored. The general structure and mechanisms are so prevalent as small molecule receptors, that a plurality of drugs target this receptor family. GPCRs basic mechanism of activation has the transmembrane receptor bound to a G-protein complex on the intracellular side of the membrane. Upon ligand binding, the G-protein complex exchanges guanosine diphosphate (GDP) for guanosine triphosphate (GTP) and dissociates from the receptor. It then activates different cellular pathways. Covering the full range of GPCRs is far beyond the scope of this thesis. However, structural data for GPCRs is particularly useful in the development of new drugs.

1.2 Microbial rhodopsins

This thesis is primarily focused on microbial rhodopsins. Like their mammalian counterparts, they have 7 TM helices and an internally bound retinal, but they do not bind G-proteins. Microbial rhodpsins can harness light for proton and cation transport, as seen in bR, hR and channelrhodopsin. Alternatively, there are sensory rhodopsins responding to the light environment, such as the well characterized sensory rhodopsin I (SRI) and SRII, and anabaena sensory rhodopsin (ASR)[26,27,28]. New microbial rhodopsins are being discovered by deep genomic sequencing[29]. Recently, the structure of heliorhodopsin was published, which shows a remarkable structural similarity to bR while only sharing 15% sequence identity[30]. Rhodopsins undergo multiple transitions upon excitation. These transitions lead to a general photocycle which undergoes K, L, M, N and O transitions. These transitions represent different structural and protonation states of the retinal which can be tracked via distinct relative absorbance shifts and can be recognized across different rhodopsins[31,32,33]. Ultrafast intermediates, I and J, have been observed both structurally in **Paper II** and via flash spectroscopy

for bR, the nature of these intermediates in the wider microbial rhodopsins is less well explored[34,35]. The Schiff base deprotonates and protonates throughout the photocycle. Photocycle lifetimes vary across microbial rhodopsins as noted by the conceit of this thesis. For the proton pump bR the photocycle lasts ~20 ms[33,36], while for the light sensor SRII the complete photocycle is ~1.2 s[37,38,31]. Indeed, the speculation that heliorhodopsin is a sensing rhodopsin is largely due to its prolonged photocycle[39].

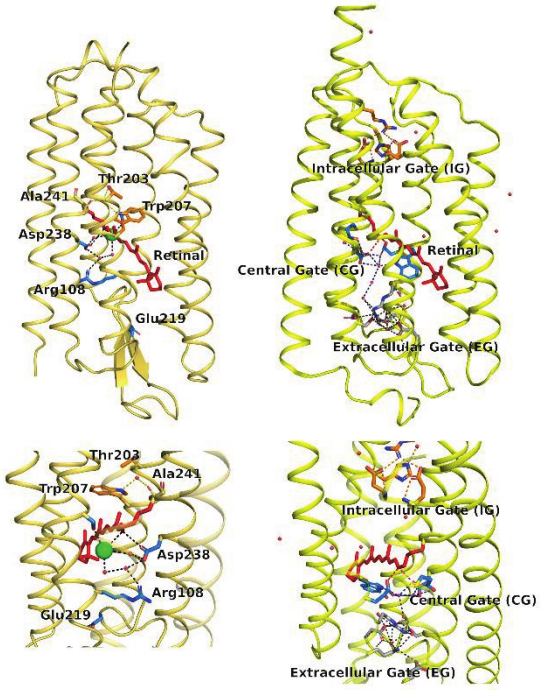

Figure 1.3, Three rhodopsins involved in ion pumping, signaling and as an ion channel displayed from the side and behind the retinal, a) Halorhodopsin, residues important residues for coordinating the chloride ion and retinal schiff base in blue, residues thought to be involved in the chloride ion release pathway in orange. **b)** Channel rhodopsin, residues for the intracellular gate, central gate and extracellular gate, and their respective hydrogen bonds in orange, blue and grey.

As this thesis focuses on SRII in comparison with bR, I will take a moment to discuss other microbial rhodopsins before exploring SRII and bR in more detail. That the microbial rhodopsins could pump large ions was demonstrated by florescence and pH measurements on hR [40]. This inward chloride (Cl^-) pump has an absorbance maxima at 575 nm, and a photocycle lasting roughly 20 ms, passing through several intermediate steps[41]. The Cl^- movement occurs in the inverse direction to protons in bR. The hR resting state structure revealed the Cl^- next to the protonated Schiff base, so in the ground state Cl^- appears to be trapped halfway through the membrane (Fig 1.3a). Isomerization therefore reverses the protonated Schiff base dipole, pulling Cl^- past the retinal[42,43]. During pumping, an inward C-helix movement prevents further Cl^- uptake during excitation[44]. Interestingly, mutating asparagine 85 (Asp85) to threonine in bR allows translocation of Cl^-, demonstrating the electrostatic subtlety of the ionic gate in microbial ion pumps[45].

Channelrhodopsins are a family of cationic specific channels[46]. Channelrhodopsin-2 (Ch2) is a Ca^{2+} specific ion channel. Light triggered cationic channels have garnered huge interest due to their ability to depolarize nerve cell membranes upon illumination[47]. Channelrhodopsins are important tools in optogenetics and research on the nervous system[48]. Recently, the structure for Ch2 has been solved to high resolution (Fig 1.3b)[49]. The structure revealed three potential gates for Ch2: a central gate around the retinal, an intracellular gate and an extracellular gate. The channel itself appears coordinated predominantly between helices A, B and G. The ordered water molecules below the retinal as seen in bR and SRII are not present, instead similar water coordination occurs via glutamate and glutamine residues that are positioned next to the Schiff base. These residues participate in extensive hydrogen bonding with waters and other residues in the putative extracellular channel. Channel opening via isomerization likely causes significant H-bond network disruption. Cavities throughout the protein would be opened by this rearrangement via a disturbed hydrogen bonding network and a straightening of helix-B[50]. Therefore, isomerization

disrupts H-bond networks, opening pre-existing cavities in the protein allowing cation transfer[49].

1.2.1 Bacteriorhodopsin

The most well studied microbial rhodopsin is bR. This protein acts as a proton pump, harnessing light energy to generate a proton gradient utilized for ATP generation. Initial studies on the purple membrane that could be extracted from *H. halobacterium* deduced the role of proton translocation and the overall photocycle[33]. In these membranes, bR forms a triangular trimer with other bR protomers[51]. This highly ordered natural array means that bR became the focus for early biophysical and structural studies[51] and it was one of the early high-resolution membrane proteins crystallographic structures[52]. Given this, and the ease of light activation, it became a model protein for unravelling the process of ion transport across the membrane.

The bR photocycle follows the typical rhodopsin photocycle, with the addition of initial I and J states. The initial ultrafast movements occur within a few 100 fs leading to transitions in the I through K states which occur during retinal isomerization[53,54]. The L intermediate precede the retinal deprotonation, and represents preparation for the Schiff base deprotonation. Freeze trapping the L intermediate revealed slight C-helix deformation, a movement that brings the retinal Schiff base and Asp85 counterion together[55]. This is consistent with deprotonation occurring in the L-to-M transition. An earlier structure revealed that the Asp85 was located within hydrogen bonding distance from Thr89, but not the Schiff base itself[52]. This suggested a transient proton transfer via Thr89 for deprotonation, which was confirmed by TR-SFX studies[56]. In the bR structure, arginine 82 (Arg82) did not appear to form a salt bridge with Asp85 as thought, but structural movements after activation suggested some role upon activation[52]. Later data revealed that proton release is carried out by an interplay between waters, Arg82 and the glutamic acid 204 (Glu204) – Glu195 pair as suggested by freeze trapped M-state and flash spectroscopy[57,58]. Later intermediates describe the

EC channel opening and re-protonation of the Schiff base. This is tied to an E-F helix opening which connects a proton wire via Asp96 to the retinal Schiff base, defining the M to N transition. Finally, there is an isomerization back to the trans-retinal and then the ground state (the N to O transition) [59]. The ground state therefore has a protonated Schiff base which will be transferred upon the next excitation event. bR therefore displays a characteristic photocycle and a series of residues and structural movements, that have become the benchmark for other microbial rhodopsins.

1.2.2 Sensory rhodopsin II and transducer

The majority of the work in this thesis covers the light sensing microbial rhodopsin SRII. In archaea, SRI and SRII work in tandem to control the cell's directed movement away from harmful near-UV light. Motility is afforded by flagella, a cellular propulsion system. In the same way that humans have adapted to avoid or mitigate harmful light such as UV-rays (< 400 nm), so too have single cellular organisms. Like humans, the simplest method is to move away from harmful light.

The early assay for SRI and SRII function was whether cells stopped their directed swimming upon illumination[26,60]. SRI appears to have two modes, responding to different light wavelengths. A photo-attractive signal is transmitted at ~565 nm, while the ~370 nm state undergoes a slow decay that produces a photophobic response[26,61]. SRII activation at 498 nm increases the photophobic response. Therefore, as the cell's light environment switches to near-UV blue, the SRI attractive signal weakens from photophobic response from SRII. Once into the UV range, the long-lived ~370 nm intermediate in SRI becomes a photophobic sensor. The two receptors therefore work together to produce an overall transition from photo-attractive to photophobic signals as the light environment moves into the UV range.

SRI and SRII both work in require transducer proteins to transmit signals. HtrII appears to bind SRII adjacently in the membrane with high binding affinity (Fig 1.4)[62]. This dimer then binds another dimer via HtrII;

therefore, the complete biological complex appears to form a 2:2 dimer of homodimers. Recent negative stain electron microscopy data suggests that this 2:2 dimer itself forms trimers in a similar fashion to bR in the membrane[63]. The SRII-HtrII signalling complex is a two-component system, with a similar architecture to chemotaxis receptors. The transducer proteins for SRI and SRII are 500-700 amino acids in length and extend into the cytoplasm. Upon activation, structural changes induced by isomerization propagate from the rhodopsin to the transducer. This signal causes a conformational shift in the transducer[64] in SRII-HtrII this phosphorylates a kinase protein, which in turn phosphorylates a complex at the base of the flagella motor[65]. This breaks and the coordination between individual flagella is disrupted and the cell stops concerted directional movement[66].

The SRII structure was revealed to be remarkably similar to bR, and unbound to its transducer protein SRII intrinsically acts as an inefficient proton pump[67]. Meanwhile, attempts to convert bR to transmit signals showed that it requires only three mutations to confer basic signalling function, A215T being the most significant of these[68]. The other two

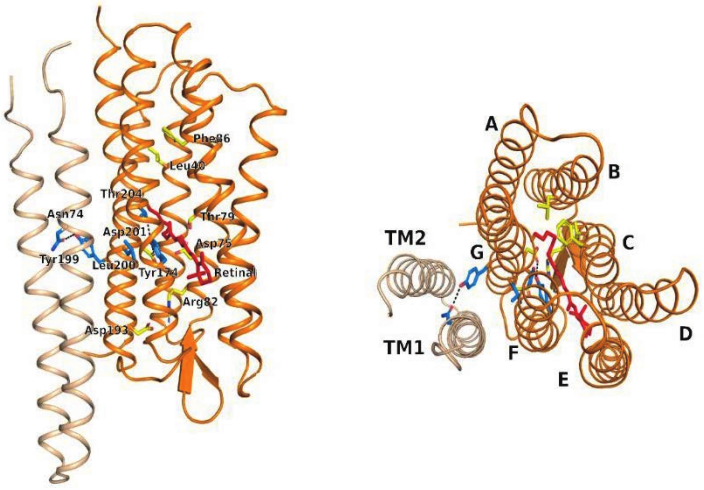

Figure 1.4, Structure of the complex, the structure of the complex, the receptor in orange and the transducer is white, yellow residues are involved in pumping while the blue residues are involved in signal transduction. The display from above shows the relative positions of all the helices.

mutations for converting bR into a sensory protein are along the TM-helical interface. Therefore, the similar overall structure and small to no requirements for different functionalities indicates that large differences in structural mechanism are unlikely. Some insight can be gleaned from the SRII photocycle, thus its relevance to functionality and dynamics has been the focus of intense study. The photocycle for SRII has presented some discrepancy over different measurements. However, a general mechanism from is laid out in Fig. 1.5 is likely. The explanation for measurement discrepancy is possibly due to buffer conditions. Some studies have indicated significant pH insensitivity between 5.5-9[31]. Furthermore, Fourier-transform infrared spectroscopy (FTIR) has shown that the Asp75 counterion does not change its pH between pH 5-8[69]. This differs to measurements of the M and O state decay at higher salt concentrations[70]. Furthermore, M-decay is accelerated in the presence of azide, suggesting that reprotonation drives M-state decay and directly relating the M state to the protonation state of the Schiff base[71]. This confers with the observation that O decay is not governed by Schiff base reprotonation, but by retinal and protein effects[70,69]. For SRII there is a discrepancy whether there is an N state in the photocycle, since (as for pH sensitivity) the low salt concentration shows an N-like intermediate while higher salt FTIR studies do not[31,70].

The driving force behind SRII function is the retinal isomerization. For SRII, femtosecond spectroscopy reveals that isomerization appears similar to bR and hR, but elicits a slightly different response from the protein post-isomerization[35]. This is consistent with a model for signal transduction, where a steric class between carbon number 14 (C14) and the tyrosine 174 (Tyr174) – Thr204 hydrogen bond transmits a signal to the transducer. The steric clash does not seem to occur when Thr204 is mutated to alanine (Ala), cysteine (Cys) or serine (Ser), but is present in the signalling triple bR mutant[72]. FTIR reveals that the Thr204 hydrogen bonding that changes upon activation, are also influenced by transducer binding[73]. This hydrogen bond is shifted during the K state and strengthened during the M state[73]. These structural changes are thought to propagate to the transducer via Y199 on helix-G[74]. This highlights a key role in early signal transmission for Thr204.

Structural evidence, however, puts more weight on an F-helix tilt seen by FTIR and cryo-trapped crystallographic intermediates as the main form for signal transduction[75]. The crystal structure showed no major structural rearrangements that are induced upon transducer binding. NMR results, however, found subtle changes on the E and F loops and around the chromophore binding pocket[76]. Furthermore, increased thermal stability is conferred by transducer binding, indicating a general stabilizing effect[77]. The binding affinity between even shortened constructs is ~200nM[62]. Curiously, binding becomes significantly worse when the transducer is truncated from 114 to 82 residues. X-ray structures only show residues 22-85, therefore the segment responsible for tight binding is not stable enough to be observed crystallographically[75]. Upon activation, like other rhodopsins there is an outward helical shift[37,78]. Crosslinking studies confirm that this outward movement likely interacts with the adjacently positioned transducer[79]. This

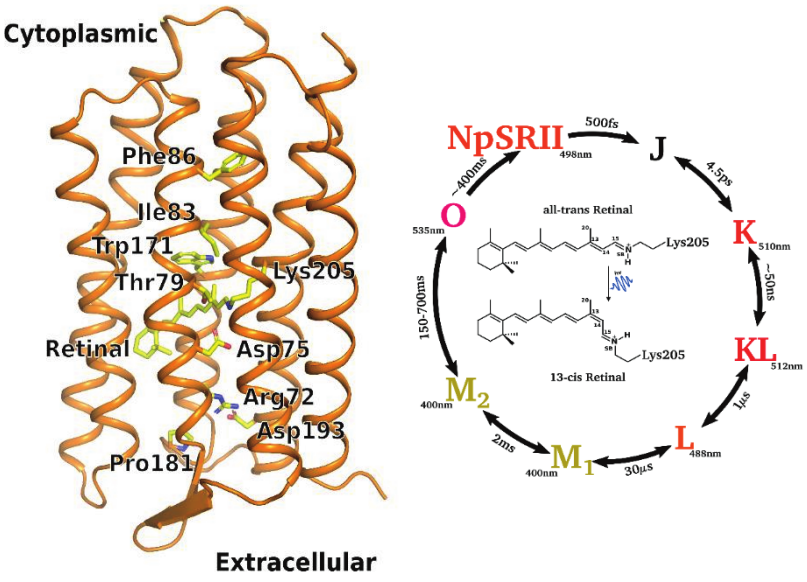

Figure 1.5, Structure of sensory rhodopsin II, SRII structure with the complete photocycle.

outward shift has been attributed to the late M state following volume

changes in SRII and complex[80]. Transducer binding appears to slightly slow the decay of the M state in the SRII-HtrII photocycle[80]. Recently, the publication of a new crystal form has suggested another mechanism for signal transduction[81]. The authors defined their new crystal form as a U form in contrast to the already published V form. They proposed that signal transfer was carried out by a rack and pinion mechanism that shift from U to V. This would push the transducer upwards, in contrast to the rotational twist previously suggested[81]. This does explain the observations that the EF helical loop plays an important role in receptor transducer interface[82,83].

1.4 Scope of the thesis

This thesis aimed to explore the structural rearrangements in microbial rhodopsins with particular focus on SRII from *Natromous pharaonis* and its cognate transducer HtrII using new methods in time-resolved crystallography. This is of particular importance now due to the possibility to compare with recent high-resolution TRX structures of bacteriorhodopsin. Moreover, SRII-HtrII complex has many structural similarities to chemotaxis receptors in prokaryotes, potential drug targets.

In **Paper I**, new crystallization conditions for SRII and SRII-HtrII are used with new microcrystallisation strategies to produce large volumes of crystals for serial experiments. This is the first reported structures for SRII and SRII-HtrII that do not include purple membrane addition to crystalize.

In **Paper II,** ultrafast time-resolved crystallography was used to track retinal isomerization in bR. This revealed distinct structural intermediates during this ultrafast process before completing isomerization. This study pushed the boundaries of TRX studies by measuring at the fastest time-resolution made possible by XFEL sources.

Paper III, captures a light-activated intermediate state via TR-SMX crystallography in SRII. This is an early study for room temperature membrane crystallography at a synchrotron. This revealed differences in the helical movements that occur during the proteins excited state and provided

a structural explanation for the extended photocycle lifetime when compared to bR. The work highlights the possibility for synchrotron sources with relatively little adaptation to collect structurally relevant time-resolved data at room temperature.

Paper IV highlights a low-resolution structure for SRII-HtrII solved by room temperature serial crystallography. New crystallization conditions provided SRII-HtrII crystals outside of purple membrane reconstitution. Extra helical density was resolved on the TM helices not typically available to crystallography. This study shows the possibility to study prokaryotic signalling with high temporal and spatial accuracy at room-temperature, which would provide definitive answers to open questions in the field.

In **Paper V,** TR-XSS experiments are carried out on SRII and with added transducer, following previous work on rhodopsins via TR-XSS. This showed an EF-helical transition that is perturbed by the addition of transducer protein. This provided good evidence for a potential signal transduction mechanism. Furthermore, it provides a starting point for advances in modelling TR-WAXS data.

2. Membrane protein crystallography

2.1 Purification of membrane proteins

As outlined in Chapter 1, membrane protein crystallography has played a key role in understanding the molecular mechanisms and how cells

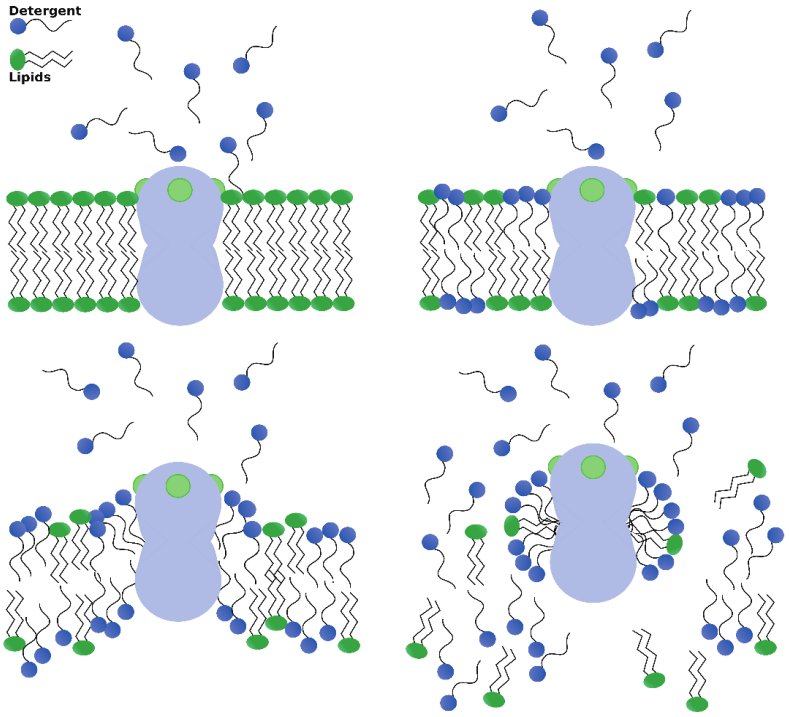

Figure 2.1, Protein solubilsation, The detergent intercalculates between the lipid molecules degrading the integrity of the lipid bilayer and forming a new hydrophobic core around the protein.

adapt to their environment. Membrane proteins are therefore attractive targets for structural biology. Expressing, purifying and crystallising these proteins is far from trivial, due to the requirement to replace the membrane, which stabilizes the hydrophobic transmembrane regions. Membrane proteins are extracted from the membrane by solubilization with detergent

molecules which form a micelle around the protein (Fig 2.1). While detergent-protein stability has to be optimized for each membrane protein, once a stable buffer has been selected the membrane protein is typically amenable to most standard purification methods. The other major candidate as a substitute membrane is purified lipids. Detergent solubilized SRII is sometimes reconstituted into the purple membrane lipids that surround bR[84,85]. Recent methodologies have also reconstituted membrane proteins in lipid-nano discs, thought to provide a more accurate bilayer analog[86].

2.1.1 Protein expression

While proteins are expressed in a natural host cell, the quantities are commonly insufficient for biophysical experiments. The great success of molecular biology in the last 40-50 years has been developing methodologies for protein cloning and over-expression in non-host organisms[87]. Cloning techniques allow the protein encoding gene to be inserted into a plasmid or vector and to be expressed by a non-host organism. The protein expression system within the cell is recruited to carry out, transcribe, translate and, for membrane proteins, insert into a membrane.

Considerations for host selection include expressing the protein in a similar organism to the source organism, so that there is an appropriate molecular machinery for expressing the target protein. Previously published protocols had success in expressing both SRII and a truncated $HtrII^{1-114}$ in *E. coli* cells[88], a commonly used host organism for prokaryotic proteins. Both proteins were expressed in *E. coli* cells strain BL21(DE3) with a pET28a vector with a T7 promoter. This is a widely used expression system using isopropyl-β-D-thiogalactopyranoside (IPTG) to induce expression. Protein harvesting requires cell lysis, to either extract the lysate for soluble proteins or the membrane fragments for membrane proteins. Cell lysis is achieved, chemically via enzymes, mechanically via excess pressure or by sonication. SRII and $HtrII^{1-114}$ underwent sonication to disrupt the cell membranes via liquid sheer pressures for the TR-XSS experiment. The TR-SMX data was collected on sample broken mechanically.

2.1.2 Solubilisation

Transmembrane proteins sit across the lipid bilayer. This dielectric barrier needs to be replaced with a mimic in order for the proteins to be stable when removed from the membrane. Detergents are amphipathic and can intercalculate into a membrane. High detergent concentrations effectively dissolve the membrane and forms micelles (Fig. 2.1). Each detergent has a critical micellular concentration (CMC), where micelles form spontaneously which is clearly important to surpass during solubilsation. Different membrane proteins are sensitive to different detergents. To ensure the protein is reformed, the detergent and its concentration are optimized for successful solubilisation. SRII is stable in multiple detergents[88,89]. Crystallization has typically been successful in n-Octyl-β-D-glucopyranoside (BOG), which has a CMC ~0.7% w/v[109]. Therefore, SRII and HtrII the fragmented membranes were pelleted by ultracentrifugation at 220,000g and were resuspended and solubilised using 4%w/v BOG overnight at 4°C.

Stable protein in detergent is an important step in purifying and studying any membrane protein. However, legitimate concerns regarding whether the detergent micelle provides an accurate reflection of the lipid environment has incentivized performing experiments in liposomes or lipid discs. In SRII, solubilisation shows slight changes in the decay rates in the M-decay[90]. Furthermore, the equilibria between the M and O states changes in the solubilized form compared to lipid resuspension[90]. Importantly, purple membrane lipids are required for larger oligomers. The full complex is not observed in detergents and we have modelled in our data accordingly (**Paper IV**).

2.1.3 Chromatography

Protein chromatography separates proteins based on their physiochemical qualities. Common considerations are the overall charge, a specific tag, or size. The sample can be passed over a column with chemical characteristics selective for the protein of interest. Anion and cation

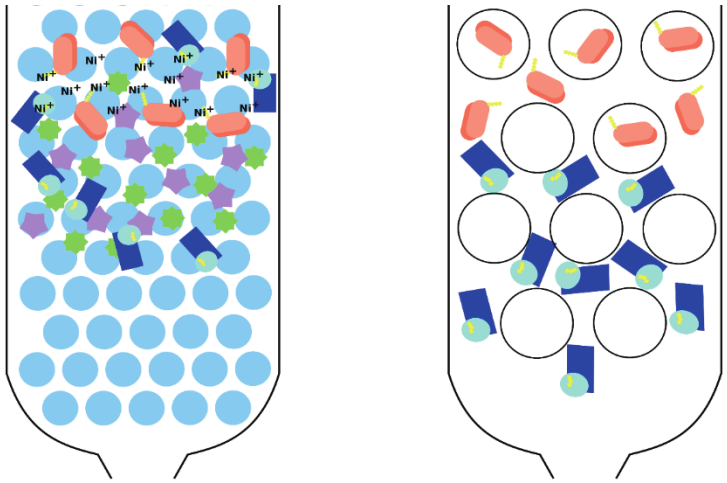

Figure 2.2, Protein chromatography, Representations of both nickel ion affinity column and size exclusion. Both methods where used in this thesis to purify SRII and HtrII.

columns, for example, bind a protein dependent on the proteins overall charge. Therefore, changing the pH of the buffer during binding and elution will separate the protein of interest from other proteins with differing isoelectric points. Here, SRII and HtrII$^{1\text{-}114}$ have 6 histidine residues added to the N-terminal. The histidine coordinates metal ions, therefore a column with a resin bound to nickel provides a strong interaction with the tag, hence immobilized metal-ion affinity column (IMAC) Figure 2.2. Other proteins with histidine rich-regions will also bind. In this thesis, both proteins where purified with a his-tag and nickel affinity column (Ni-NTA). Two wash buffers where passed over the column to remove non-specific binding proteins with the second containing 40 mM imidazole (a histidine analogue that outcompetes protein binding at high concentrations). The protein was then eluted with 160 mM imidazole solution.

After the initial column, SRII contained an impurity with a 420 nm specific peak and was therefore not pure enough for crystallization. The sample was run over a size-exclusion column. As implied, this column separates the protein by molecular weight, which is achieved as the column matrix is hollow and prevents proteins over a given size from entering. Larger proteins must travel a shorter distance because they cannot enter the beads. The proteins too large to enter beads exit the column first, with the eluting protein then become smaller until they are too small for effective

separation (Fig. 2.2). Sample homogeneity can also be assessed from an even elution peak. For both SRII and HtrII, a single HiLoad 16/600 Superdex 200 pg column was run and fractions with a 498 nm absorbance (SRII) or showed ~12 kDa bands ($HtrII^{1-114}$) were collected and crystallized.

2.2 Crystallization

2.2.1 What are crystals?

A crystal can be simply defined as an ordered arrangement of molecules. Crystals exist for single atoms to complete protein molecules. This ordered arrangement of molecules represents the solid state for many materials as laid out by Lawrence Bragg in "The Structure of Silicates"[91]. The response to these chemical conclusions from early X-ray experiments were not met with universal approval as this, rather amusing, quote from a letter to nature indicates[92]:

Prof. W. L. Bragg asserts that "In sodium chloride there appear to be no molecules represented by NaCl. The equality in number of sodium and chlorine atoms is arrived at by a chess-board pattern of these atoms; it is a result of geometry and not of a pairing-off of the atoms". This statement is more than "repugnant to common sense". It is absurd to the nth degree, not chemical cricket. Chemistry is neither chess nor geometry, whatever X-ray physics may be. Such unjustified aspersion of the molecular character of our most necessary condiment must not be allowed any longer to pass unchallenged. A little study of the Apostle Paul may be recommended to Prof. Bragg as a necessary preliminary even to X-ray work [...], that science is the pursuit of truth. It were time that chemists took charge of chemistry once more and protected neophytes against the worship of false gods; at least taught them to ask for something more than chessboard evidence.

-Professor Henry E. Armstrong

Despite this almost biblical criticism, the false gods of crystallographic diffraction prevailed and the technique is now widely

accepted for determining the atomic coordinates of the constituent molecule. X-ray crystallography has therefore developed into a major materials science technique with particular success in determining the structure of proteins.

2.2.2 Crystal growth

The most difficult process in protein crystallography is growing a protein crystal. Crystallization is driven entropically, while the protein ordering produces a large positive ΔS this offset by a negative ΔS for the precipitant solution, normally forming the protein water shell, becoming disordered during crystal formation. Crystallization is thus a careful balance between the entropic relationship between solute and solvent. This explains why crystallization precipitation buffer is so important. Proteins have large and complicated architectures and to form crystals, these structures must make regular contacts with each other. These crystals contacts are weaker and further apart then in small molecule crystals. Therefore, protein crystallization is a careful balancing act between the protein and buffers entropic forces. Given this, protein crystals are typically fragile. Growing crystals is typically done by making small changes to the protein concentration *via* vapor diffusion using many different solutions. In this thesis, most crystals were grown in lipidic cubic phase (LCP), however the most common crystallization methods and theory will be briefly discussed before addressing LCP.

As outlined, the relationship between the buffer constituency and protein concentration is crucially important in growing crystals. In essence, crystallization can be thought of as controlled precipitation. What makes up this precipitant solution is crucial but it is difficult to predict what will produce crystals. Therefore, large crystallization screens are required to sample a wide range of conditions. During a typical crystallization experiment, vapor diffusion is used to navigate the crystallization diagram and encourage spontaneous nucleation. As outlined in Fig. 2.3, the crystallization diagram hypothesizes that some protein and precipitant

concentration ranges enables crystal nucleation and growth. In a successful crystallization, a shift in protein concentration pushes the system in a nucleation zone. Crystals grow from these spontaneous nucleation points decreasing protein concentration as molecules are incorporated. Crystals are enlarged until the system moves out of the growth phase.

Finding a good crystal condition is a difficult process. Membrane protein crystallization may be affected by pH, reagents present, the detergent chosen, temperature, protein concentration, precipitant concentration, the precipitant chosen or the container in which crystallization is carried out. Furthermore, variation between different purifications can change the crystallization. Attempts to rationalize crystallization conditions[93] have achieved some success in assisting crystallization. For membrane proteins. LCP places the membrane protein in

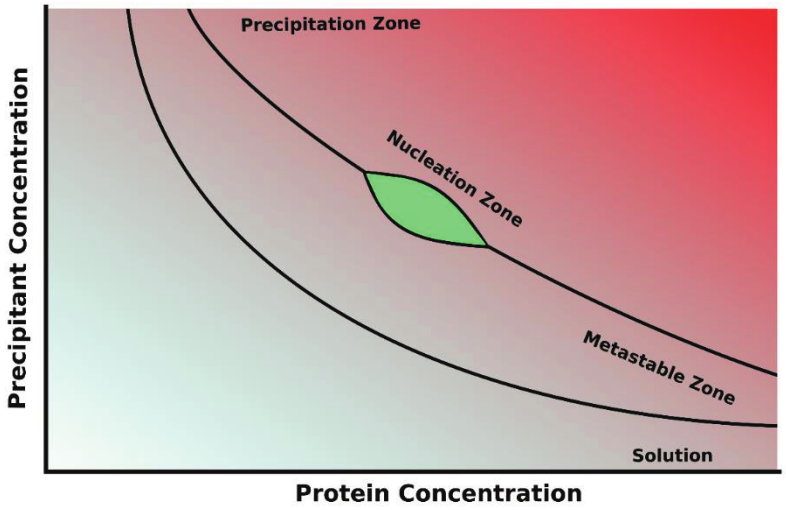

Figure 2.3, Crystallization diagram, A diagram representing the different zones that can be navigated by a crystallization experiment. As the protein concentration is altered by vapor diffusion or dilution. A successful experiment hits the nucleation zone and produces spontaneous nucleation points that grow into crystals as the protein concentration is reduced. The protein can enter the precipitation zone. Here the protein crashes out of solution and form an unusable precipitation.

a lipidic environment that facilitates a more stable platform for nucleation. All crystals in this thesis were grown in LCP.

2.2.4 Lipidic cubic phase

LCP refers to a specific phase that a lipid-water system can form given that the correct water:lipid ratio is mixed together at a specific temperature. Lipids respond differently and form different phases at different ratios that need to be mixed to achieve a given phase. The most common lipids is monoolein, which has a well elucidated phase diagram and forms lipidic cubic phase upon mixing with water in a 40:60 water: lipid ratio[94]. As monoolein is solid at room temperature, it is heated to 40°C before mixing. Preventing the monoolein becoming solid before mixing is vital for successful LCP formation. Concentrated protein solution as the aqueous phase can be mixed and thereby incorporate the protein into the LCP. LCP has a dense viscous consistency commonly compared to toothpaste. This is due to the unique architecture that the lipids form, which comprises a folded bilayer structure with water pores running throughout[94]. The membrane proteins can sit in these bilayers and have translational movement. This allows the membrane proteins to be bought closer together in a more stable platform to form crystallization nucleation sites.

Despite the more amenable environment available to membrane proteins in LCP, crystal growth is still driven by precipitation buffers. Unlike vapour diffusion methods, moving around the crystallization diagram (Fig2.3) is achieved by adding precipitant solution to the LCP. This allows the solution to diffuse into the LCP changing the proteins local environment and driving crystallization. SRII and SRII-HtrII$^{1\text{-}114}$ were both grown in monoolein LCP. Successful reconstitution is typically identified by the LCP transparency after mixing the two phases. For SRII the LCP was not consistently transparent, however this did not stop crystal growth. Furthermore, for SRII-HtrII, complex crystals from **Paper IV** had 5% (v/v) phytantriol added to the molten monoolein.

2.3 Paper I: Well-based crystallization for serial crystallography

A major aim for this thesis was measuring SRII and SRII-HtrII by serial crystallography where many small crystals are required, in contrast to the typical desire for large crystals. Obtaining these crystals has been the focus of some research [95,96,97] . In **Paper I,** we describe a method for producing showers of microcrystals in LCP. Previous approaches focused on producing these crystals in vials or syringes, both being filled with precipitant solution and an LCP string. The crystallization focuses for SRII and truncated transducer, was to produce crystals of the SRII-HtrII$^{1\text{-}114}$ complex to carry out time-resolved crystallography experiments to discern the structural underpinning of signal transduction. We also realized that crystallizing SRII on its own would provide insights into both signal transduction and functionally relevant differences in the structural movements in comparison to bR.

2.3.1 New SRII crystals

Previous crystallization for SRII and SRII-HtrII[98,81] had required reconstitution into purple membrane lipids. These were typically extracted from *Halobacterium salinarum*, which presented a challenge from a sample requirement perspective. For the SRII complex crystals, producing lipids in addition to the two membrane proteins was not feasible considering the several hundred microliters required to run the most sample conservative experiments. We thus decided to rescreen without the reconstitution step. Initial screens were carried out in 96 glass well plates and dispensed with a mosquito TM crystallisation robot. This produced a hit in the Memgold2 screen[93] that diffracted to 2.6 Å and reproduced the old SRII condition. Carrying out serial experiments requires large LCP volumes with batch crystallisation producing thousands of crystals. Initial attempts to scale up were tried in syringes but were unsuccessful. In syringe crystallization, the Hamilton syringes used for producing LCP are filled with precipitant buffer

and an LCP string is injected into it. The string is therefore suspended in the precipitant solution and the syringe sealed for the duration of crystallization as outlined in **Paper II**. Initial attempts were also made with 24-well plastic plates, yielding some success. However, glass well-based crystallization produced better looking LCP after weeks in buffer and produced crystals more reliably and therefore these methods was used going forward.

2.3.2 Well-based crystallization general methodology

Well-based crystallization was carried out in rounded bottom deep glass well plates. A crystallization experiment can be run in each well or the same condition can be used in each well to produce large sample volumes. LCP is prepared, typically in two Hamilton glass syringes via standard LCP methodology[94]. Precipitant solution is pipetted into each well and LCP string is added to the well, trying to avoid crossing itself. Ideally, and if the sample is mixed well this is relatively easy to achieve, the string will be pushed out in on move and form a swirl in the well. The sample can be tethered to the side of the well or left to float in suspension. Once filled, wells are sealed with Clear-Vue plastic sheets, fixed by friction to the over the top of wells. The plate is then stored and monitored for crystal growth. Once crystals have grown, they can be harvested by adhering the sample to the end of Hamilton syringe plunger.

2.3.3 Well-based crystallization advantages

Well based crystallization had been successfully developed for and applied to cytochrome C oxidase microcrystallisation in LCP[99]. This strategy has several key advantages, in syringes it is difficult to monitor crystal growth under a microscope. Syringes are glass cylinders which causes optical distortions when trying to view the contents from outside. Therefore, to monitor crystal growth the sample has to be pressed out from the syringes disrupting the crystallization and risking sample loss. Well-based crystallization has a plastic layer placed over the well and LCP can therefore be easily visualized and the plastic removed and replaced easily for sample

handling. Secondly the sample amount in a single well is typically between 10-20 ul, therefore the volume per plate is far more than the amount contained in a syringe. Considering that both syringes and plates are approximately equivalent in cost, the well-based crystallization is considerably cheaper per unit volume. Finally, and crucially, the sample is easily harvested for beamtime as, providing the LCP does not melt into the precipitant solution, it adheres easily to the Hamilton syringe plunger. Sample is therefore wrapped about the plunger tip and compressed into a large Hamilton syringe. Multiple wells can be collected in one syringe and excess precipitant solution or trapped bubbles removed with the plunger. Removing excess precipitant solution is particularly important, as it typically improves extrusion from the injectors used in serial experiments for LCP.

2.3.4 SRII at large scale

SRII was grown in *E. coli* and harvested as has been described above in methods. For initial large-scale crystallization screens, the SRII was concentrated to 20 mg/ml (0.8 mM) and reconstituted in LCP. The well based screen varied PEG400 (precipitant) and pH, this was same as the small-scale screens, where significant differences between conditions had been observed. For batch screens, steps of 2 % around 34 % PEG400 and 0.5 pH below pH 9 were used. In our lab, large scale production of microcrystals had typically come with increased concentration of solution. The PEG concentration went further up, 42% PEG400, then down, 30% PEG400, given the initial 34% concentration. The pH range was set downward from pH 9 as better crystals where observed at more neutral pH conditions in small scale. These conditions produced crystals in a few conditions, but a greater crystal density and faster growth was observed with lower pH and higher precipitant PEG concentrations. This matched our expectations based on small-scale observations and previous experience for membrane proteins.

Despite crystals growing at large scale, the crystal density remained lower than what was likely to produce a reasonable hit rate for an injector experiment. As highlighted in the crystallization section above,

microcrystals are common when the condition hits the nucleation zone quickly since multiple crystallization sites develop simultaneously before the concentration has been altered due to crystal growth. We therefore decided to try higher protein concentrations expecting to nucleate faster and produce smaller crystals more reliably. We tested both 30 mg/ml and 40 mg/ml, the upper limit was based on successful microcrystallisation conditions for bR[56]. The same conditions at 40 mg/ml produced a greater crystal density. These were taken to the BioMAX beamline at MAXIV were they recorded diffraction to ~2.7 Å (Fig. 2.6). This condition, sample and method was used for the time-resolved serial crystallography experiments at the Swiss light source.

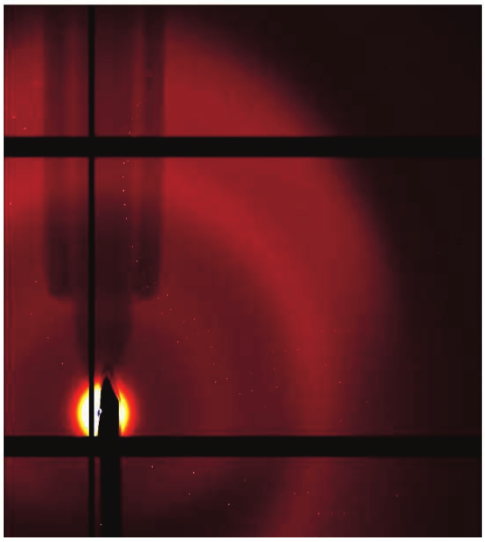

Figure 2.6, SRII diffraction from Biomax. An example of a diffraction measurement from the experiment at Biomax, MAXIV. Due to difficulties with beamline setup the sample was not possible to be successfully indexed. However, it showed the possibility for diffraction to past 3.0Å.

2.3.5 Paper I – summary

Serial crystallography requires large sample volumes containing thousands of crystals. This provides a unique sample challenge that requires optimization to produce large amounts of appropriately size crystals with

high crystal density. SRII, initially crystallized at small scale, was up-scaled to produce 100 ul sample in deep well glass plates using a technique developed in our laboratory for work on cytochrome C oxidase. After several rounds of optimization to increase crystals density and decrease crystal size, they were measured at synchrotron sources by room-temperature serial crystallography where they diffracted to higher than 3 Å resolution.

3. X-ray scattering, theory and practice

The primary experimental methods of the thesis are crystallography and solution scattering. Given this, the theory behind X-ray diffraction and scattering is central. This chapter provides a theoretical introduction to scattering theory, its application to crystallographic diffraction and the difference in data obtained from solution scattering.

3.1 General scattering theory

Electromagnetic waves can be described in terms of an electric field vector and magnetic field vector both oscillating perpendicular to the wave propagation. X-ray scattering involves the interaction between the intercepted electron cloud and the electric field of the X-rays. This interaction can therefore be calculated as the addition of sine waves, the general formulae for the multiple addition of sine waves (k) can be defined as:

$$F = \sum_{k=1} F_k \cdot e^{i\varphi_k} \qquad (3.1)$$

where **F** is the summed scattering vector, φ is the phase angle. As constructive and destructive wave theory dictates, the scattering is strongly influence by the phase angle. In this thesis we exclusively deal with elastic scattering, therefore by definition there is no energy change between

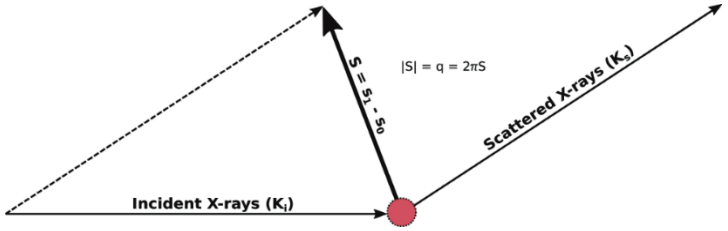

Figure 3.1, A general scattering diagram demonstrating a mathematical construction for scattering from a point

incident and scattered X-rays. This has relevance when we consider the geometric aspect of protein scattering. In solution scattering, the momentum transfer is defined as the scattering vector between the incident X-rays (k_i) and the scattered X-rays (k_s) diagrammed in Fig 3.1.

When considering the phenomena of interference, this diagram is further complicated by considering two scattering points in an electron density cloud, therefore the total scattered wave becomes a product of both scattered waves (Fig 3.1). As noted in equation 3.1, the phase contributions are considerable. The difference in the path length is directly related to the phase difference. Assuming that $\mathbf{r}$ is the vector difference between the two points then taking the dot product allows us to calculate the phase difference between partial scattering events. The path difference can be calculated as follows:

(3.2) $$\Delta p = \boldsymbol{S} \cdot \boldsymbol{r}\lambda$$

where $S = |K_i - K_s|$, from this vectoral description we can easily calculate the phase difference by multiplying by $2\pi/\lambda$.

(3.3) $$\Delta\varphi = 2\pi \boldsymbol{S} \cdot \boldsymbol{r}$$

Substituting equation 3.3 into equation 3.1 and taking the integral, we get the scattering over the volume cloud $\rho(\mathbf{r})$, or the atomic scattering factor for an atom.

(3.4) $$f(s) = \int \rho\,(r) e^{2\pi i S \cdot r}\, dr$$

An important difference between solution scattering and crystallography is that in solution scattering, the scattering vector is defined in q space. This is denoted in radians, $q = 2\pi\mathbf{S}$, therefore equation 3.5 gives us the atomic scattering factor in terms of q.

(3.5) $$f(q) = \int \rho\,(r) e^{iq \cdot r}\, dr$$

Equation 3.4 and 3.5 both represent a different form of the atomic scattering factor. The most obvious aspect about equation 3.5 is that it is a Fourier transform. Therefore, the inverse Fourier transform of the scattering waves describes the atomic distribution of the scattering particle, which in essence, is the whole point. A useful consideration here is the resolution of an experiment. In crystallography and structure determination, achieving high resolution is important to unambiguously assign positions to the chemical structure. It becomes harder to tell a definitive chemical story at lower resolution. The theoretical resolution can be seen as:

$$resolution = 2\pi/q_{max} \tag{3.7}$$

where q_{max} is the largest recorded angle of q. Obtaining a higher resolution is therefore a matter of obtaining a larger value of q. Defining q as in equation 3.8, we can see that it is possible to obtain greater values of q by increasing the scattering angle or decreasing the wavelength. The wavelength must be smaller than the difference between the two atoms that we wish to resolve and typically is less then 1Å for X-ray experiments. For crystallography experiments, sample quality (the regular and ordered nature of the diffraction grid) typically defines how good the resolution is but we can see quite clearly why spots that reach the edge of the detector mean a higher resolution for the experiment.

For all scattering experiments, only the amplitude of the scattered wave is recorded as a measured intensity. This problem in crystallography is known as the phase problem; reconstructing via similar, known structures or employing methods to experimentally determine the phases can be used to overcome it. In solution scattering experiments, the averaging of phases caused by the disordered molecules makes structural interpretation entirely reliant on testing models against the measured scattering curve. We can consider these models to be providing the phase element to any potential solution.

3.2 Crystallographic diffraction

X-ray diffraction from a crystal was first realized by Max von Laue[100]. William Lawrence Bragg built on this work, hypothesizing that crystals were layers of regularly ordered atoms and that the diffraction spots observed by Laue were produced from constructive interference between X-rays scattering off ordered layers. From this he derived the following equation:

$$n\lambda = 2dsin\theta \tag{3.9}$$

The Bragg equation describes the relationship between the X-ray beams angle of incidence θ with the crystal plane (lattice), the distance between the crystal lattice planes, d, and the X-ray wavelength, λ. This can be visualized as in Figure 3.2. When the Bragg condition is met, the constructive interference produces a Bragg peaks. This can be visualized via a second graphical construction, the Ewald sphere. Taking the reciprocal of the Bragg equation.

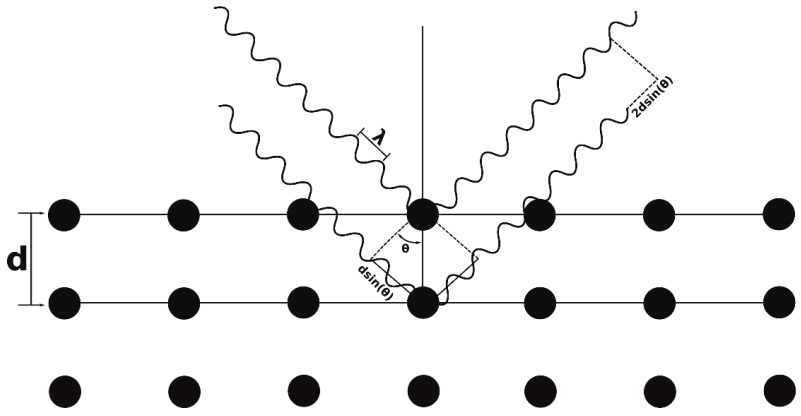

Figure 3.2, The bragg equation, a diagram representing the geometric description of the bragg equation.

(3.10) $$\frac{1}{d_{hkl}} = \frac{2sin\theta}{\lambda}$$

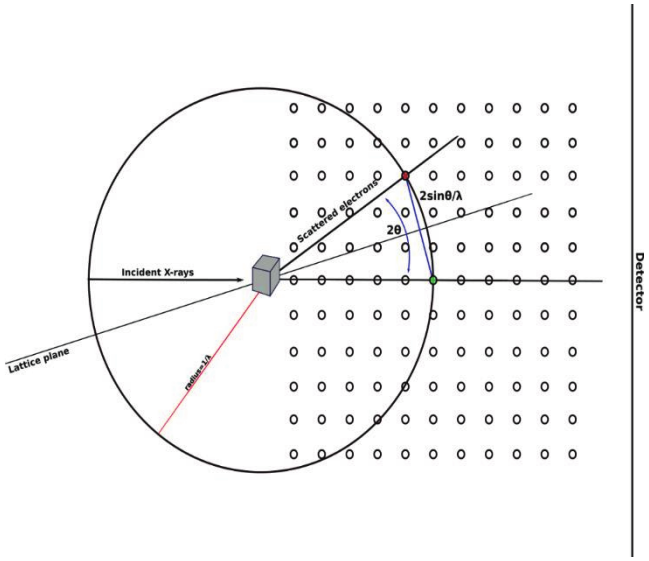

Figure 3.3, The Ewald sphere, a diagram displaying the reciprocal lattice defining the scattering angle and wavelength required for constructive interference

This construction of the Bragg equation shows that the reciprocal lattice can be directly related to the scattering angle at a given wavelength. As demonstrated in Figure 3.3, scattering vectors that bisect the Ewald sphere meet the conditions to produce coherent diffraction.

By definition all crystals are made from repeating units called the unit cell. This is the smallest repeating unit and can reproduce the entire crystal by translational symmetry. The unit cell can also contain more than a single protein. The asymmetric unit defines the unit cell by rotational and translational symmetry. For example, the SRII crystals in this thesis have only one protein in the asymmetric unit and therefore the asymmetric unit and the unit cell are the same. Real space planes are formed by these repeated proteins that in total make up the crystal. These are defined as vector indices or Miller indices (hkl). The reciprocal lattice is the reciprocal of the real space

planes. The Miller indices have a direct correspondence to the reciprocal space lattice. In order to sample the Ewald sphere, the crystals must be rotated such that the different Miller indices can be recorded. A point to note, Laue diffraction has advantages to TRX studies for the increased photons a polychromatic beam provides. From the Ewald sphere construction (Figure 3.2) it is clear that multiple wavelengths permit a greater sampling of the Ewald sphere. Recent experiments have confirmed this in serial crystallography with fewer diffraction patterns being required to collect an entire dataset[101].

Equation 3.4 defines the total scattering of a given molecule ρ(r). In the case of crystals, this scattering is convoluted with the discrete lattice sampling permitted by the hkl indices. Therefore, using the scattering function defined in equation 3.4 we can write an equation for the crystal diffraction

$$g(s) = f(s) \times \exp\left(i2\pi nS \cdot r\right) \tag{3.11}$$

where g(s) is the crystal diffraction, f(s) are the structure factors for a crystal. As scattering only occurs when the miller indices conditions are met, we can write an expression for the structure factor amplitudes from a crystal as follows.

$$F(hkl) = \sum_j f_j \exp\left[i2\pi\left(hx_j + ky_j + lz_j\right)\right] \tag{3.12}$$

As mentioned, scattering only measures the intensities of scattered reflections. These scattered intensities are the squared magnitude of the structure factors amplitudes. It is trivial to regain the structure factors amplitudes from the measured intensities however this contains no phase information. As we know that the inverse Fourier transform of the scattered waves describes the scattering object and that the square root of the measured intensities are structure factor amplitudes, which in turn are the amplitudes of those scattered waves. What is still required is the phase

information. Nevertheless, an equation for electron density calculation from experimental data can be given as follows:

$$p(x,y,z) = \frac{1}{V}\sum_h \sum_k \sum_l |F_{obs}(h,k,l)|\cos\left[-2\pi i(hx + ky + lz) + i\alpha(h,k,l)\right] \quad (3.13)$$

The F_{obs} contains the measured structure facture amplitudes, the phases as defined by the second term can be experimentally measured or they must be reconstructed during data processing and refinement.

3.2.1 X-ray crystallography data analysis

The primary step in crystallographic data processing is determining the space group and unit cell parameters. Several different indexing programs exist, the primary indexers used in this thesis are XDS[102], DIRAX[103] and XGANDALF[104]. Indexers also try to correct for background and produce a series of observed intensities across hkl indices. The dataset can then be merged and scaled, as each hkl is measured several times at different orientations. The measurement precision during the experiment can also be assessed. The crystallographic standard is R_{merge}. Increased R_{merge} indicates more precise peak measurement, but as it correlates with number of times a peak is measured is difficult to use as an indicator of data quality. For this thesis scaling and merging was done by the programs indexamajig and paritalator from the program suite crystFEL[105]

Once the crystal is indexed and data merged and scaled into a set of hkls, the phase problem can be addressed. Phases can either be taken from a similar structure that has already been solved or measured experimentally. Using a similar starting structure is called Molecular Replacement and which uses a Patterson function to place the candidate structure in the unit cell. Rotation and transposal movements are made to improve the statistical likelihood that the structure is a better fit to the data. Experimentally determined phases are directly calculated from the anomalous scattering of heavy metal atoms either added to the sample or already part of the

structure. With this phase information we can update equation 3.14 to include the input potential phases and generate an initial electron density map.

3.2.2 Crystallographic refinement

After initial phasing, the electron density map needs to be analysed and adjusted manually. The entire structure may need to be modelled *de novo*, regions might need to be remodelled or amino acids changed and fitted. The program COOT is designed to carry out this modelling in real space and even slight manual adjustment can improve the overall fit[106]. This adjusted model can then be used to generate a new set of phases and the maps recalculated. Refinement programs also try to produce a better fit by modelling occupancies, rigid body fitting and other computational methods. To avoid overfitting, the R-factor and R-free is recalculated after each round of manual refinement.

$$R_{factor} = \frac{\sum_{hkl}||F_{obs}(hkl)|-K|F_{calc}(hkl)||}{\sum_{hkl}|F_{obs}(hkl)|} \quad (3.14)$$

where K is a scaling factor. As the phases from the model are used for the next calculation, it is possible to overfit the R-factor. Typically, 5% of reflections are withheld from refinement and used to calculate the R-free (R-factor calculation using withheld reflections). Usually the R-factor is 2% better then R-free. Improvements to R-factor without R-free is assigns of overfitting particularly greater the 2% deviation. R-factor typically refine to 15-20% for high resolution datasets.

3.2.3 Conventional cryo-crystallography

Conventional crystallography experiments use monochromatic X-rays through a crystal which is rotated to record all the Miller indices that produces a dataset. The monochromatic beam samples a small amount of the Ewald sphere. This data scheme therefore collects multiple images from a

single crystal. The radiation exposure for a crystal during data collection is a problem and the sample is therefore cooled to 100K for data collection[107]. The advantage of this method is that the angle of incidence is accurately recorded, making the determining the crystal parameters, indexing, relatively easy. Furthermore, the single wavelength means that the detector is not saturated with diffraction spots. For simply determining the protein structure, Laue diffraction methods hold no benefits, making this the predominant method for structural solution in crystallography.

3.2.4 Serial crystallography – new rules

Serial crystallography collects thousands of partial diffraction patterns by passing many crystals past the beam. The crystal orientation is considered random and each Bragg peak is measured multiple times. The sample delivery methods can be divided into two groups, fixed target matrix and injectors. Fixed targets matrices load small crystals onto some form of grid, which is then raster scanned across the beam path collecting images at each grid point. Injectors pass crystals in a stream through the X-ray beam. Liquid injectors use crystals grown via hanging drop and loads a concentrated slurry of crystals. The requirement for a laminar flow makes liquid injectors particularly sample consumptive and therefore less attractive then LCP injectors. Recently, however, methodologies for reducing the sample consumption via acoustic droplet delivery have been published[108]. LCP injectors utilize the high viscosity of the sample to produce a laminar flow. Given the prevalence for membrane proteins to crystalize in LCP makes them an attractive option. This is the primary method of sample delivery used in this thesis.

This data collection is done at room temperature. At XFELs, radiation damage is not considered due to the “diffract before destruct” theory, however, recent evidence suggests this may not be entirely true[109]. Serial crystallography at synchrotrons also seen a decrease in radiation damage, possibly due to inconsistent effect across all crystals measured[110]. The high redundancy of these measurements means that density

representing flexible loops has been recovered[95]. Setting up a simple pumped-probe delay before each crystal and the ability to collect at room temperature, makes serial crystallography very amenable to time-resolved experiments.

3.3 Time-resolved structural biology

A protein's dynamics is an essential aspect. Protein activation can alter a protein's energy landscape, allowing it to shift between different series of conformational states[2,111]. Proteins have been shown to partially sample functional confirmations even in the ground state[111]. Characterizing a protein's dynamic movement during function is essential to having a complete understanding for its mechanism of action. Protein structural biology makes it possible to resolved a protein's tertiary structure with high spatial accuracy. Conversely, as proteins are in a nanometre size range, the pre-eminent methodologies for doing this requires extensive averaging to provide measurable signal.

In crystallography, this averaging occurs because the protein is in a crystal and the signal strength is proportional to the crystal's dimensions[112]. In electron microscopy, structural determination by single particle reconstruction uses *in silico* 2D and 3D classification which is computational averaging. This means that the solved structure is an average and therefore static. Recovering the time-dimension with high temporal and spatial resolution during a proteins functional movement is the focus of time-resolved structural biology.

3.3.1 Time-resolved X-ray crystallography; lights, camera, action

The principle that protein dynamics occurs in crystals has been known since the early days of protein crystallography[113], which provides the theoretical possibility to observe enzyme dynamics in crystals. As already mentioned, crystallography inherently averages what is being measured.

Capturing protein movements requires that motions are coordinated, therefore proteins must be triggered simultaneously to allow motions to be correlated across all activated proteins. Methods for this trigger include, mixing with substrate[114,115,116] electric field stimulation[117], irradiation[118], and photoexcitation[56]. Using a laser pulse to excite an already present chromophore is well suited to these experiments, as it is relatively trivial to produce short discrete laser pulses tuned to a specific wavelength. Sample can therefore be pumped with a laser followed by a measurement pulse, a scheme called pump-probe (Fig3.3). Another consideration for measuring these transient intermediates is the need to measure a dataset within the life span of the intermediate. This limits the X-ray exposure time to being less than the measured time point. However, short X-ray pulses lower the signal to noise as an insufficient number of photons are present in the pulse to produce enough elastic scattering to measure a diffraction spot.

The first time-resolved X-ray crystallography (TRX) experiments utilized Laue diffraction which increases the number of photons by using a polychromatic (multi-wavelength) beam. This polychromatic beam also samples more of the Ewald sphere but produces difficulties in unambiguous peak assignment. These experiments were either triggered by intermediate mixing and measured over long timescales[114] or they were triggered via light illumination allowing for shorter timepoints[119,120]. In the early 2000s, synchrotrons managed to push the time resolution to a few hundred picoseconds when tracking carbon monoxide release from myoglobin[120,121]. Synchrotron Laue studies were then successfully applied to photoactive yellow protein, a bacterial photo-receptor, from nanoseconds to milliseconds[122,123]. Membrane protein studies using photosynthetic reaction centre revealed energy harnessing intermediates[124]. These studies showed what could be achieved at synchrotrons. Soon, however, a new tool entered the frame for these experiments: X-ray free electron lasers (XFELs).

XFELs are capable of producing ultra-short (fs) and incredibly brilliant pulses of X-rays. Normally this amount of radiation would destroy the sample. However, the ultrashort pulses means that diffraction outruns the radiation damage and sample explosion, known as "diffract before destruct"[125]. XFELs therefore offered the potential for radiation free structural studies of proteins at room temperature. Furthermore, the X-ray pulse (pump) is considerably shorter than synchrotrons therefore XFELs offer faster time points, better spatial resolution and room temperature dynamics. Given this, time-resolved studies on proteins using XFELs have had remarkable success. Work started at the synchrotrons has been advanced, catching the new intermediates in photoactive yellow protein [126] and intermediates in myoglobin carbon monoxide dissociation[127]. Considerable advances in energetic proteins have been made, in particular landmark

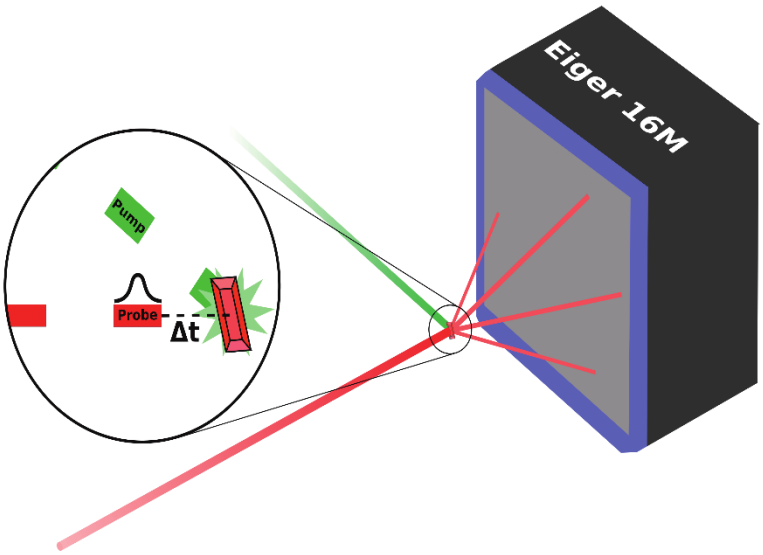

Figure 3.4 Pump-probe setup, Classical pump-probe setup for time resolved crystallography. The difference between the pump and the probe (Δt) defines the time-point in the reaction. Both the Pump and probe have a determined pulse length, the Δt cannot be shorter than the either the pump or the probes length.

studies in bacteriorhodopsin[59,56,128]. Experiments have been carried out on photosystem II to follow reactions in the radiation sensitive oxygen evolving centre [129,118,130]. The terminal oxidase cytochrome C oxidase and P450 oxidase have also been adressed[99,131]. The pace and interest in these studies shows that it is beginning to be applied as a general method for understanding a proteins functional mechanism rather than being the purview of a few bespoke crystallographic groups.

While the biological understanding garnered from XFELs has been considerable, the requirement for continuous sample delivery and complete dataset reconstruction from partial diffraction patterns has produced remarkable methodological breakthroughs. Serial crystallography is no longer confined to XFELs and is used widely at synchotrons[59,116]. **Paper II** of this thesis is a good example. Time-resolved crystallography now has a wide range of approaches for studying protein dynamics, at different sources. That slower intermediates can be measured at synchrotron sources will reduce the need for competitive XFEL beamtime. With further advances in triggering systems, a wider range of proteins and scientific questions will be answered by TRX.

3.3.2 Time-resolved millisecond serial crystallography with LCP jets

Recent successful TR-SMX experiments have been performed at synchrotrons[59]. In **Paper III** we measured a light activated-state structure for SRII in LCP at a synchrotron at room temperature. Utilizing the millisecond readout of the detector limits the time resolution to milliseconds, but the setup is relatively simple for a standard microfocus beamline. A delay generator between the detector and a Class3B laser was used to turn the diode on and off in time with detector readout. Time-resolution is determined by the detector and so detector readout is the theoretical limits of the experiment. Furthermore, a large sample volume can be pumped and measured multiple frames can be collected on the same pumped sample producing slow flowrates and low sample consumption.

In Our experiment we utilised a strategy to generate a light activated state by continuously pumping the sample as it passes the beam. This was interleaved between dark and light collection periods. This produce a well features excited state map. These experiments are particularly impressive given the single-to-noise is very low due LCP scattering.

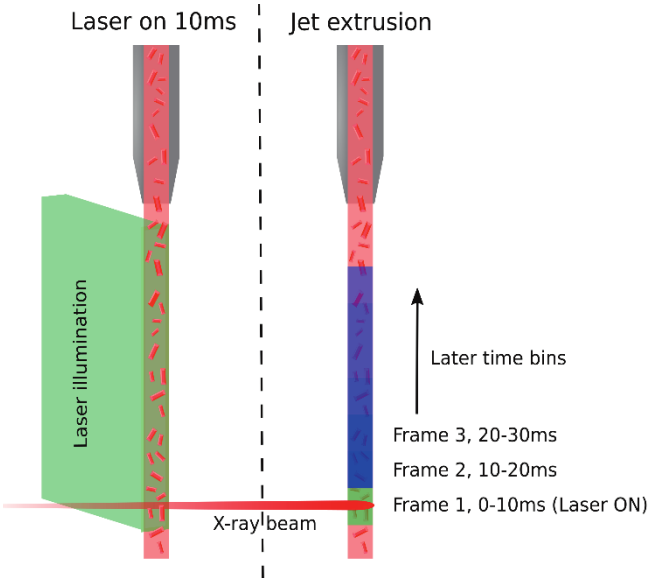

Figure 3.4, TR-SMX setup, a pump-probe setup for serial crystallography at synchrotrons. Membrane protein crystals suspended in LCP are fed from a GVDN injector into the beam path. A large section of sample is illuminated time-bins are collected as the sample passes

3.3 Solution scattering

The scattering from a concentrated protein sample works on the same fundamental scattering principle as crystallography. The primary difference is that the sample is completely disordered. Here I will briefly cover the theory of XSS.

3.3.1 Solution scattering theory

The XSS field denotes the scattering vector in terms of q, as has already been commented on above. Here q can be defined as:

$$q = \frac{4\pi sin\theta}{\lambda} \quad (3.14)$$

The nature of q here is important as it describes the relationship between the wavelength λ and the scattering angle θ. As the scattering angle increases, the scattering changes in correlation to the size of ordered elements in the system such as overall protein fold and secondary structure. XSS is radially isomorphous such that the scattering can be radially averaged into a 1D-scattering curve. This creates a function of intensity against the scattering angle q.

XSS on a sample of interest requires a contrast against the solution and or membrane for a given biological system. The atomic scattering factor can be repurposed to give the total scattering of a particle in solution, with terms to describe the contrast between the protein and bulk solvent:

$$f(q) = \sum_j \left(f_j - \rho^o v_j\right) \exp\left(iQ \cdot r_j\right) \quad (3.15)$$

where f_j is the scattering amplitude from the atom j at r_j and the sample is surrounded by the homogeneous solvent ρ^o and v_j is the volume of the atom. All scattering experiments only measures intensity of the scattered wave. The intensity is determined when the scattering factor is multiplied by its complex conjugate.

$$I(q) = F(q)F(q)^* \quad (3.16)$$

Unlike crystallographic experiments, the intensity is not the product of an ordered lattice that diffracts only upon meeting Bragg conditions. The Debye equation relates the atomic scattering factor with an

intensity for a given angle q, for spherically averaged and phased averaged samples as it scatters. This is what is experimentally measured.

$$I(q) = \sum_m \sum_n (f_m - \rho^o f_m)\,(\mathrm{f_n} - \rho^o v_n)\,\frac{sin(qr_{mn})}{(qr_{mn})} \qquad (3.17)$$

where m to n can be seen as separate atoms, r_{mn} the vector between those atoms. The formation of the Debye equation includes the contrast amplitudes as specified above. As a final point about scattering in solution the scattering intensity can also be described in terms or scattering amplitudes as below:

$$I_N(Q) = N\langle |\boldsymbol{F}(\boldsymbol{Q})|^2 \rangle \qquad (3.18)$$

Here the $\langle\,\rangle$ brackets denote rotational averaging over the square of the scattering amplitude. The scattering extent varies dependent on the correlated structural elements in the sample. We can think of q space as the reciprocal of real space, therefore at q of 0.1, structural correlation at 0.1/1 or 10Å can be observed. Such low q ranges measure effectively via SAXS measurements, and are used to define protein envelopes. Secondary structure information is encoded between 0.25 to 0.6 $Å^{-1}$, where correlations in β-sheets and α-helices predominate[132]. At higher q, the scattering is dominated by water and there is no significant correlation [137]. In this thesis solution scattering is primarily used to measure structural changes in SRII and SRII-HtrII. I will introduce the theory behind this methodology before talking about how we treat this data.

3.3.2 Time-resolved wide-angle X-ray scattering; lights, contrast, action

Protein crystals have two difficulties, firstly they are difficult to produce and secondly crystals are in an artificial environment. X-ray solution scattering provides the opportunity to study protein dynamics in solution. Time-resolved WAXS (TR-WAXS) studies at synchrotrons have been successful at tracking protein dynamics, initially with fairly well characterized sample such as myoglobin[132]. Further studies combined this with time-resolved small-angle X-ray scattering (TR-SAXS) to simultaneously reveal overall and secondary structure changes[138]. Ground-

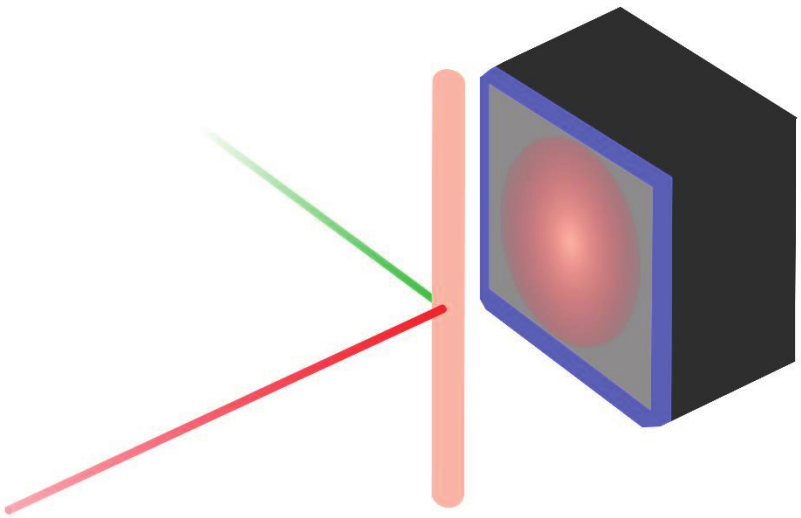

Figure 4.4 TR-WAXS setup, pumped probe setup, concentrated protein sample is flown through a quartz capillary. Several radial scattering patterns are averaged on the detector before readout.

breaking work extended the method to membrane proteins, a particularly difficult proposition considering that most membranes are placed in a micelle or bilayer. The interaction between these two are challenging to successfully model and account for. Nevertheless, application to a wide range

of rhodopsins has been demonstrated for hR[43],bR[139] and in using a homology model as a basis proteorhodopsin[140]. Recent studies showing that TR-WAXS can also be applied to XFELS, which provides exciting possibilities for both time-resolved and structural determination via solution scattering at ultra-bright sources[141,142]. **Paper V** in this thesis extends synchrotron rhodopsin studies by TR-WAXS to SRII and SRII-HtrII, looking at both rhodopsin signalling and transmembrane protein complex dynamics via TR-WAXS.

TR-SXX experimental setup requires the sample to be pumped in front of the beam. A capillary is constructed to allow a controlled flow, although fast flowing jets have been used[141]. As rhodopsins return to a ground state, the sample can be passed in front of the beam path several times. Multiple diffraction events are integrated on the detector before an individual image is readout. This means that each image will have measurable signal while avoiding saturating the detector. Difference curves are calculated from images on pumped sample against dark. These difference curves are averaged until the noise has been significantly reduced.

3.3.3 Difference scattering

As has been outlined in previous publications on TR-WAXS the theoretical implications in difference intensity calculations explain what we can read into a WAXS difference curve[132,43]. Time-resolved WAXS scattering on proteins involve either activating or exciting the protein sample and measuring with a predetermined time-delay. Once data has been collected, radially averaged, rejecting outliers and calculating the scattering is a relatively straightforward process using the following equation.

$$\Delta S(q)_{exprmt} = S(q)_{excited} - S(q)_{ground} \tag{3.19}$$

The varying intensities across the difference curves are caused by different sizes of movement in the sample. The low q region 0.1-0.25$Å^{-1}$ q represent changes in the overall protein shape. The detector distance is set to effectively measure the protein region 0.25-0.6$Å^{-1}$ q. Here secondary

structure changes are most clearly observed both in relation to different secondary structural elements, and between amino acids within a helix or sheet. At high-q scattering becomes dominated by water scattering.

Multiple difference curves are calculated across logarithmically displaced timepoints. SVD analysis across these timepoints produce time-independent basis spectra, representing the intermediates that appear. This can be further analysed via kinetic decomposition to determine the relative populations of intermediates at each timepoint. To understand what motions have occurred we can test candidate movements, calculating the scattering from ground and potential excited states. Scattering is calculated using the program CRYSOL[133] and calculating a theoretical difference curve. This calculates a solvent and vacuum terms for the scattering. The solvated term tries to account for the proteins' ordering of water by introducing a solvation term, while the vacuum calculation assumes only the atoms given. Difference scattering from membrane proteins requires further terms to account for similar problems to water order caused by the membrane. Applying these cross-terms appropriately, it is possible to account for the scattering interactions convoluted in the protein q-range ~0.25-0.6Å. For membrane proteins, this is predominantly the micelle and surrounding solvent. A better description for the scattering not caused by protein structural changes allows a more accurate modelling process.

To model these changes, candidate structural changes are derived either crystallographically or through a combination of modelling and molecular dynamic simulations[134,135]. In this thesis, 3 initial difference curves were calculated from theoretical scattering and scored. A Nedler-Mead search algorithm[136] was applied. Structural movements were chosen on helix C, observed in SRII and taken from the structure in **Paper III**, and helix-EF taken from recent TR-SMX structures of bR[59]. Structures are exaggerated by an integer value evaluated and recalculated. This is repeated until a solution has converged.

4. Sensory rhodopsin II and bacteriorhodopsin

The main focus of this chapter is to outline the work on TRX of the two retinal proteins reported in this thesis. Time-resolved studies on bR proceeds this work, however **Paper II** provides the clearest picture on the structural movements in retinal isomerization. Utilizing the ultra-short pulses provided by XFELs, seven nominal time points were collected, five covering the first picosecond, one at 10 ps and a final at 8.33 ms. This produces a clear picture of retinal isomerization in bR and a general mechanism for retinal isomerization in microbial rhodopsins. Furthermore, it elucidated how protein environments control photo-induced responses. In **Paper III** we measured later structural changes induced over longer timescales for SRII and compare them with similar measurements done for bR. This showed similar water disordering below the retinal as seen in the ultrafast measurements. However, overall map comparisons showed different F-G helical movements between SRII and bR. We analyse this result in the context of what has been seen in bacteriorhodopsin in both ultrafast measurements and millisecond crystallographic experiments recently reported.

4.1 Paper II: Ultrafast study of retinal isomerization in bacteriorhodopsin

4.1.1 Ultrafast measurements

bR crystals were grown in LCP (MAG7.9) and the experiment was carried out at the Linac Coherent Light Source. bR crystals were light adapted with 300 mW illumination for 5 min. Crystals were then injected into beam path using an LCP injector (Arizona design)[143]. The sample was pumped with

a 50 fs XFEL pulses at 120 Hz. The sample was flown at 2.5 µl min^{-1} from a 75 µm nozzle. The sample was pumped with a Ti:Sapphire laser producing 100 fs pulses at a 529 nm wavelength with a 17 µJ pulse. The laser repetition rate was 30 Hz; therefore, four images were collected after each probe. The first image was offset from the probe laser pulse by the nominal time delay (-500 fs, 300 fs, 600 fs, 900 fs, 1100 fs and 10 ps). The precise time difference was recorded with the timing tool which reported a 150 fs jitter on the timing measurement. The second pulse was 8.33 ms after the initial laser pulse. The fourth XFEL pulse was used to produce a large dark dataset over the experiment. The diffraction images were sorted using the program cheetah, indexing and merging was carried out with indexamajig and paritalator respectively from the software suite CrystFEL[105]. Crystals diffracted in $P6_3$ hexagonal space group with a resolution of 1.5Å for dark and 1.9Å for light time points. Ultrafast measurements were binned into 18 snapshots on the fs scale. Isomorphous difference maps were calculated for all timepoints against the total dark dataset using a refined dark state to produce the excited state maps.

4.1.2 Ultrafast retinal isomerization

The earliest difference density map (0-142 fs) revealed that isomerization starts with the Schiff base nitrogen shifting toward the G-helix. Negative features appear along the retinal on even carbons between 8 and 12. Evidence suggests that there is an early charge relocation in the retinal from Schiff base to the β-ionone ring. That these negative features are clear on the retinal double bonds suggests that the retinal is trying to sample isomerization points. That other points are considered for isomerization but that retinal isomerization is consistent to a give double bond strongly suggests that the chromophore binding pocket influences the bond choice for isomerization. At the 457-646 fs, strong negative features on the C20-C13=C14 bonds suggests the retinal twists at the isomerization point. During this time, surrounding C=C bonds twists in the opposite direction to the main C20-C13=C14 movement. This twist continues out to 10 ps map where the

isomerization has occurred. However, the retinal is twisted from a planar configuration with the C20-C13=C14 isomerization site is heavily towards the G-helix. The final 8.33 ms map shows the retinal having straighten and projected upwards.

4.1.3 Immediate water disordering

A universal feature to microbial rhodopsins is the water cluster below the retinal. The almost immediate nitrogen schiff base movement towards helix-G is correlated with a downward movement in water 402 (Wat402). This movement has strong correlated positive and negative density for Wat402 over the entire first picosecond (Fig4.1). This is required for lowering the energy barrier to isomerization. Negative features also appear for the entire water cluster and slowly dissipate over the first picosecond. This could reflect a protein quake that has been observed in other proteins and over similar timescales, which acts to disperse molecular energy caused by excitation.

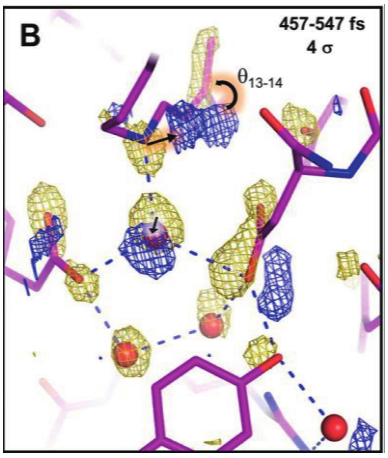

Figure 4.1, ~500fs intermediate in retinal isomerization, as the retinal twists in opposite direction we can see immediate water disordering. A negative density is observed on the Tyr182 residue important in SRII signal transduction.

4.1.4 Implications for SRII

The retinal in SRII does not possess the identical position as bR, a noted fact when the structure was first published[98]. This contributes to the spectral shift from a 570 nm to 498 nm between the two proteins. In SRII, the nitrogen is positioned slightly closer to Asp212 which contributes to the absorbance spectral shift[144]. This is itself caused by a slight inward displacement in Helix G for ground state SRII. The current mechanism for signal transition is based around a steric interaction between C14 and Tyr174-Thr204 hydrogen bond breaking[145]. This disrupts a hydrogen bond network that eventually breaks the hydrogen bond to the transducer through Tyr199. In bR, the retinal isomerization causes a twist on the C20-C13=C14 bonds that positions them twisting directly towards Tyr174. This strongly supports a mechanism that at least initiates structural changes through breaking the Tyr174-Thr201 hydrogen bond[72,145].

4.2 Paper III: SRII, time-resolved millisecond crystallography

After retinal isomerization, rhodopsins propagate changes through the tertiary structure. Recent publications have tracked these later structural changes in bR using TR-SMX. In order to do a successful comparison with a signalling rhodopsin, crystals for SRII were grown in monoolein without lipid reconstitution. The SRII signalling was measured at room temperature, the sample underwent constant illumination during data collection. This was then compared to bR data collected in the same way. We can therefore compare functionally relevant structural changes in the later structural intermediates. In bR, these movements are linked to reprotonation of the Schiff base[59] while for SRII these states constitute the signalling state.

4.2.1 Data collection and handling

SRII crystals were grown in a novel condition without reconstituting the protein into membranes. Large LCP volumes were

obtained by crystallizing 10 µl LCP containing SRII in deep glass plates as outlined in **Paper I**. Crystals took approximately 1-2 months to grow. In total, approximately 200 µl crystal containing LCP was taken to the PX1 beamline at the Swiss Light Source. The sample was tested for its ability to create a stable jet at the PSI, optimization determined that 20% additional monoolein was needed to ensure stable jetting. Sample was loaded into a 20 µl reservoir and was jetted from a 75 µm nozzle at 0.05 µl/min. This meant that one reservoir ran for approximately 6 hours. The sample was continuously illuminated with a Class3B laser diode with a 488 nm wavelength overlapping with the X-ray focal point. Laser illumination continued for 30 mins, the diode was then turned off and dark images were collected for a further 30 mins. The final processed hit rate was determined to be 1%. This was repeated until roughly 20,000 images were collected for both the excited and dark state.

Data processing was carried out in the program CrystFEL, initial indexing without specifying space groups revealed a different unit cell and P centric space group. Attempts to index this space group where unsuccessful and the diffraction was limited to 3.5Å. Further data collection revealed a second distinct sub-population within the sample which diffracted in C2221 with the old SRII unit cell parameters to ~2.1Å. The dark state was subjected to multiple rounds of refinement in PHENIX. From this, an isomorphous difference map was calculated using structure factors, $|Fobs_{light}| - |Fobs_{dark}|$, in PHENIX[146]. This meant that the experiment had a low overall hit rate, but with the low sample consumption a strong difference map was produced after ~24 hours data collection. An earlier study on bR utilized a time-resolved setup, were the laser diode was flashed for 5 ms and then data was collected for 100 ms afterwards in 5 ms time bins. This experiment was performed on the SRII crystals with 10 ms flash and a 250 ms readout, a time interval corresponding to M to O transition. After processing these maps, it was evident that a laser overlap had occurred and therefore this data could not be reasonably interpreted.

4.2.2 Overall map comparison

The excited state SRII map showed correlated positive and negative features above 3σ. The strongest feature was located on the Helix-C at ~6σ. Correlated features on the retinal and the tryptophan above and below shows an upward trajectory, which had been observed in bR. Therefore, this map clearly represented structural movements. Considering the movements present in helix C, and that there were features present on Helix-F, we concluded that this structure likely represented the signalling M state in SRII. To reveal structural differences between bR and the TR-SMX excited steady state, a difference map for bR from a previously reported experiment was

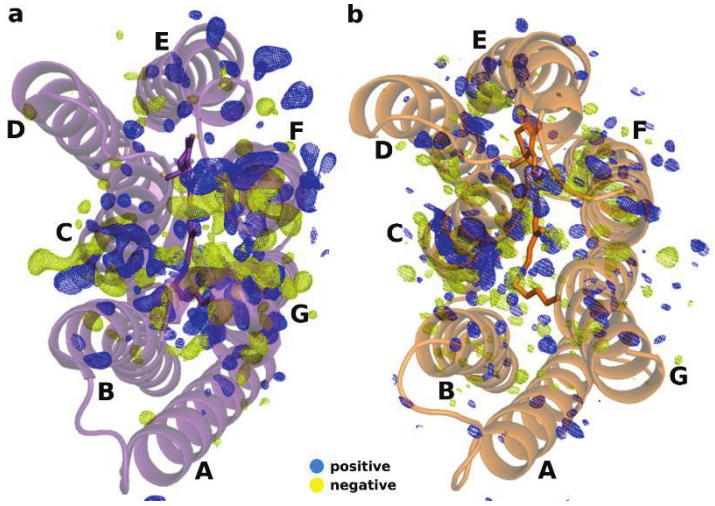

Figure 4.2, Overall comparison between bR and SRII, The electron density across both the SRII and bR steady state difference maps. The distinct differences between bR and SRII on the G helix with reduced difference density on this helix.

calculated[59]. Comparing helix movements between the two maps showed a similar inward movement on Helix-C. On Helix-F there was considerable negative features along the helix in both cases, the positive density was not as strong but still present (fig4.2). TR-SFX and TR-SMX have seen both movements before in bR. SRII is consistent with a theory posited about these structurally similar microbial rhodopsins that isomerization leads to a movement on helix-C and an outward movement on helix-F. These

movements have also been seen in cryo-trapped studies[74,147], EPR[37,148] and TR-WAXS[139], for bR and SRII. Helix-G is where the two structures diverge. In bR this helix moves inwards towards the retinal while helix-F moves out. In SRII, Helix-G does not show any significant movements along this helix.

4.2.3 Hydrogen bond coordination on Helix-G

To understand this reduced movement in helix G, we can take a closer look at the retinal, the surrounding waters and residues. As observed in the 8.33 ms map in **Paper II**, the retinal had a strong feature on the C20 and

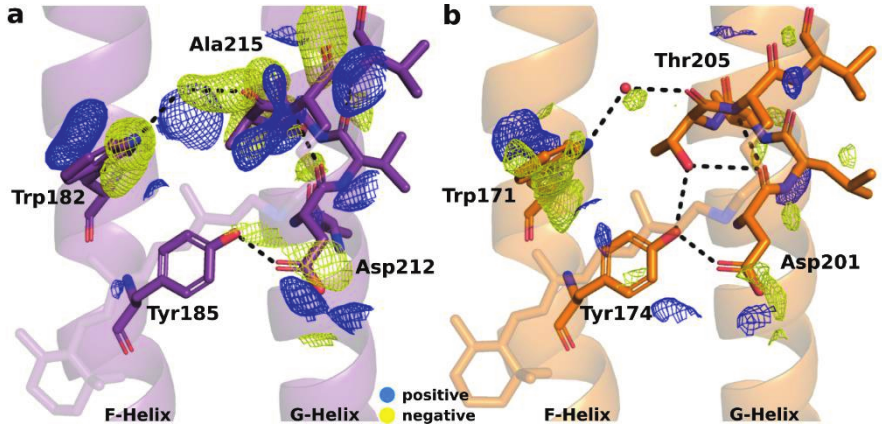

Figure 4.4, Inter-helical movements between F and G helices, the loss in clear density features on Helix-G is clear while Trp182 continues to move upward showing no loss in helix movement on helix G. Thr204 provides more rigidity to the helical movement then Ala215 in bR holding closed the reprotonation channel.

an overall upward trajectory. There is a coordinated water between Helix-G and Helix-F in both proteins. Trp181 and Trp171 in SRII and bR, respectively, follow an upward trajectory. These tryptophan's are hydrogen bonded to this water with the carbonyl oxygen on Ala215 or Thr204 coordinating the water on the Helix-G (Fig4.3). As already mentioned, the Thr204-Trp171 hydrogen bond flexing and breaking is the initial signal transfer to the transducer. Our data suggests that it also limits the movement of Helix-G during excitation. This is in agreement with FTIR data suggesting that this hydrogen bond is

present but weakened in the M-state[145], indicating an active role for the Tyr172-Thr204 hydrogen bond in excited state dynamics. The T204A photocycle produces an extended M-state and a weak O-state formation[149]. A triple mutant that makes the EC proton refilling and a cytoplasmic proton release group similar to bR produces similar early state kinetics to bR, but with an extended O-state decay. Adding T204A mutant reduces the O-state decay from 160 ms to 40 ms[149]. Our data suggests that this residue influences the opening and closing of the EC side by limiting the structural change and lengthening time of the movement. Therefore, threonine extends the signalling state life time a characteristic feature of sensory rhodopsins and an understandable need for signal magnification.

4.2.4 Disorder waters and proton gating

The water dissociation seen upon retinal isomerization is clear in both maps. This is expected as a characteristic feature in the rhodopsins. In bR, Asp85 acts as the protonated Schiff base counterion. TR-SFX studies details a rearrangement after the proton transfer in a possible charge

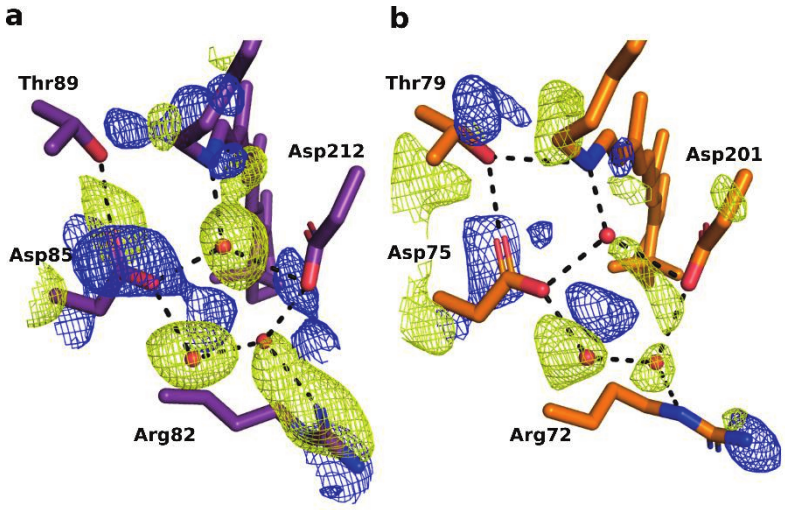

Figure 4.3, Water disordering between microbial rhodpsins, Water disordering is similar between both SRII and bR. The residues around the amino acids display distinct differences, with reduced movements on Asp85 and Arg72 indicating that dynamics no longer optimize protein pumping movements.

transfer redistribution[56]. This rearrangement is clear in the bR map but not evident in the SRII excited state. SRII is an inefficient proton pump without its cognate transducer[6762]. The movement in bR ensures proton translocation is unidirectional by preventing reprotonation of the Schiff base. Therefore, lack of this movement points to SRII inefficiency being the lack of the conventional gating mechanism. Thr89 is thought to facilitate the charge transfer process. In the SRII dark state Thr79 maintains a hydrogen bond to the Schiff base nitrogen. Thr79 shows a strong upward shift which is in accordance with the Helix-C movement already observed. Upward movement suggests that the Thr89-Asp85 hydrogen is stretched during photo-activation, confirmed by FTIR[145]. The proton gating mechanism in bR is not maintained in SRII dynamics and movements in these residues are driven by Helix-C movement, decreasing the proton pumping efficiency. Arg82 in bR moves downwards which facilitates proton release, in SRII this residue is already in this position. Arg72 in SRII still plays a role in proton release and plays a role in chromophore tuning.

4.2.5 Mechanics

These two studies provide a new picture on the mechanics and functional adaptations in the retinal rhodopsins. The retinal isomerization takes ~1 ps and starts with the Schiff base nitrogen moving towards Helix-G, concurrently disordering the water mediated hydrogen binding network below. Meanwhile, the extended retinal samples potential isomerization points before isomerization at C13=C14. This process in turns causes retinal to shift out of and back to a planar configuration. In bR, this isomerization provides the structural perturbation to induce the F and G helices to move in opposite directions while Helix-C shifts inwards after the proton translocation. Finally, F and G helical movements complete the opening up of the proton channel and the Schiff base is deprotonated. In SRII, the Helix-C moves inwards, but only Helix-F moves. Helix-G shows little movement therefore the proton refilling channel does not completely open the later

states are therefore extended as the due to the hindrance of schiff base reprotonation.

5. SRII and transducer

A complete understanding of signal transmission by SRII requires structural studies with it in complex with its transducer, HtrII. Differences caused by transducer binding are subtle and make no difference to the protein's optical absorbance. However slight structural differences due to binding have been observed by nuclear magnetic resonance spectroscopy[150]. A key aim was producing high resolution crystals of the complex. While we produced SRII-HtrII crystals[114], they did not diffract to high resolution. We did however manage to produce a low-resolution structure. This showed good agreement with the published structures for the U configuration[81]. The high redundancy from serial crystallography recovered additional helical turns on the transducer. This work paves the way for time-resolved crystallography on SRII-HtrII at both synchrotrons and XFELs. As crystallisation is non-trivial, TR-XSS experiments allowed the elucidation of the helical transitions in signalling without crystallisation. SRII difference scattering showed similarities with previous work on bR. In bR, these features correlated to C and EF-helical movements shown in crystallographic data[56]. The addition of the transducer saw a reduction in the second protein peak in the difference curves. Kinetic analysis revealed a single intermediate which was fitted against crystallographic shifts from SRII (**Paper III**) and recent bR TR-SFX studies. Transducer addition caused reduction in the outward helical shift, probably due to an interaction with the transducer helix TM2 (Fig1.4).

5.1 Paper IV: serial structure of SRII-HtrII

5.1.1 Crystallizing the complex, archaeal lipids

So far, all crystal structures for the complex have required both transducer truncation and reconstitution into purple membrane lipids[84]. As

outlined in 2.3.1, we were not able to produce the purple membranes, we decided to use the truncated construct but not reconstitute the protein into liposomes. Initial screens produced a condition for SRII, but not the complex. We theorized that the lack of lipid reconstitution may be hindering complex formation and crystallization. Therefore, we decided to incorporate a lipid additive that could act as a substitute for the missing lipids. Lipid reconstitution is supposed to provide a native environment, so to simulate this we decided to dope the monoolein with a lipid with similar chemical structure to archeal lipids. Archeal membranes are distinct as the primary lipid, archeol, contains an isoprenic tail. Fortunately, this is similar to the tail group for phytantriol (Fig5.1). Phytantriol also forms a similar phase diagram to monoolein with only a slight alteration in the ratio for LCP formation at

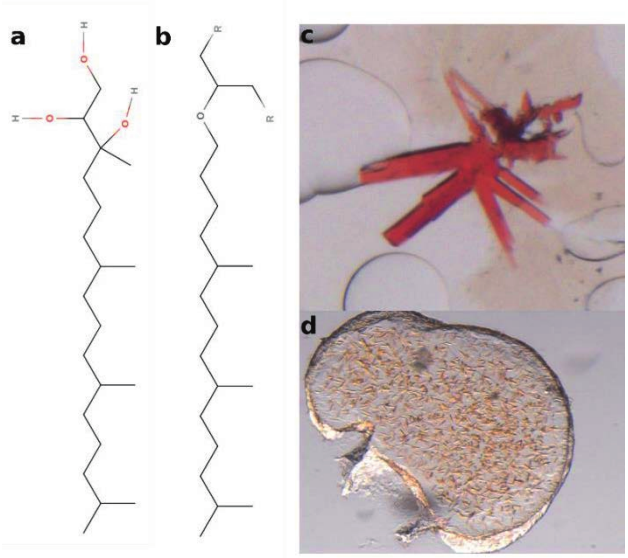

Figure 5.1, Phytantriol and early crystal structures, a) Molecular structure of phytantriol with isoprenic tail group b) Molecular structure general archaeal lipid displaying similar tail to phytantriol. c) Crystal from the initial condition producing low resolution SRII-HtrII by cryo-crystallography. d) Microcrystals of SRII-HtrII

20°C. Therefore, we doped the LCP with 5%, 10% and 15% (v/v) phytantriol by

mixing with the molten monoolein. Small scale screening revealed a condition that diffracted to low resolution, but upon molecular replacement with SRII reproduced positive density for the transducer. Having developed crystals for the transducer, we set about optimizing them at small scale and large simultaneously. These crystals did not grow as well at large scale. However, the condition that yielded well diffracting SRII crystals, when optimized for large scale, also produced large scale complex crystals. It was therefore this condition that was collected on at SLS in May 2019. This resolved a slightly lower resolution complex structure at ~5Å. While this condition requires improvement for well diffracting crystals (some of which are already being tried), the presence of complex crystals in this new condition provides an exciting opportunity to perform time-resolved serial crystallography on this model signalling complex.

5.1.2 Serial crystallography

SRII-HtrII crystals took approximately 2-3 weeks to grow to completion, this was faster than the SRII crystals despite lower resolution diffraction. Data was collected at the PX1 at the Swiss Light Source, crystals were injected via an LCP injector at approximately flowing at ~250 μm/s. Data was collected on an Eiger16M detector in 4M mode with 50 Hz repetition rate for a 0.02 s X-ray exposure. The X-ray beam was focused to 20 x 5 μm beam with the X-ray energy the diffraction patterns were indexed and merged using the program CrystFEL[105]. In total, approximately 14,000 diffraction patterns were collected and produced a unique space group and cell dimensions to our previous cryo-structure in $P222_1$. As had been seen during other serial experiments, indexing with unit cell limitations in CrystFEL produced a few different viable indexing parameters. SRII-HtrII has shown a variability in the unit cell dimensions and, less commonly, space group. Therefore, to determine the correct unit cell parameters, each one was tested and the CrystFEL statistic analysed, with C centred parameters producing reasonable indexing and statistics.

Molecular replacement was performed initially in C222, this produced a weak molecular replacement with inconsistent density. We therefore allowed phase to include other space groups which produced a stronger solution in C2221 and re-indexed the data set in C2221 for further refinement. Molecular replacement in C2221 was done with both U (5JJE) and N (5JJV) confirmations from recent publications. The U confirmation (R-factor/R-free, 0.2980/0.2731) produced a better R-factor upon refinement then the V confirmation (R-fac/R-free, 0.508/0.486). This was reflected in the crystal packing which was thought to be key for producing the different crystal forms due to the effect on the transducer protein. To confirm that the crystal structure was SRII-HtrII and not SRII, the transducer was removed and refined against the SRII only. The molecular replacement solution reproduced positive helical density for the transducer protein with identical crystal packing. This was strong evidence that the structural solution was correct and was showing the complex. Therefore, further refmac refinement was done with the U-confirmation and extra helical turns where modelled from the positive density observed in early maps. These did not improve the R-factor and R-free considerably, something attributed to the low resolution.

5.1.3 The serial structure density

The serial structure for SRII-HtrII agrees well with the previously reported structures[151,81]. As the resolution is lower than previous structural solutions, this is to be expected considering phase contributions. Despite this the preference for one of the two, SRII-HtrII crystal forms and the reappearance of transducer density when phased with SRII indicate that the replacement solution is not merely phased noise. Helices are unambiguously placed with the typical rhodopsin 7-TM helical circle, surrounding an internally bound retinal weakly represented in the density. The helices are bound adjacent in the membrane plane, opposite to helices F and G with a slight diagonal offset. Comparison with the cryo-crystal structure reveals the serial density has a less clearly defined helical twist and side chain density. This is attributed to the variations between the measured crystals increasing

the noise of the dataset which is the merged into a total dataset. This is reasonable considering that the crystallographic statistics suggest that diffraction is measured beyond 4.2Å, although the statistics do not support a consistent dataset beyond the 4.2Å cutoff limit. This in turn is reflected in observations during the experiment, suggesting that the crystals fragmented during sample preparation. This is likely to have caused increased variation in diffraction quality across the crystals.

5.1.4 Extra helical density

One particularly interesting feature in the serial structure is the extension in density on the two TM helices. This density is lost in all cryo-crystallographic structures and is reported to be dynamically flexible between two distinct confirmations[83]. Serial crystallography is premised on

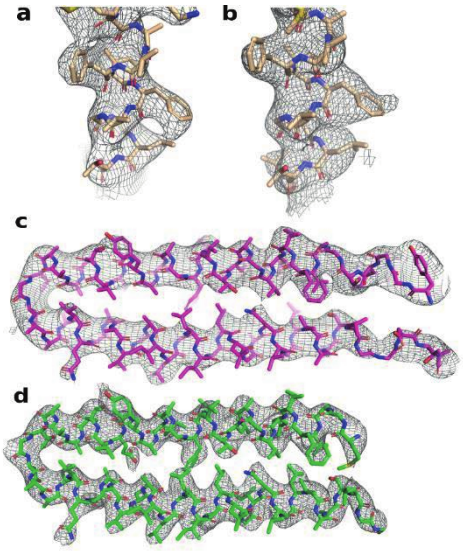

Figure 5.2, Density representation from the different structures, a) Helical turns from the transducer from the cryo-crystallography density, b) Helical turns from the transducer from the serial crystallography density c) Serial helical density for the transducer from serial crystallography d) Serial helical density for the transducer from cryo-crystallography

collecting thousands of randomly ordered partial diffraction patterns until a

statistically redundant dataset is created. Given this, serial crystallographic datasets have redundancies of typically between 100-1000 for particularly large datasets[95,128,56]. This has been shown to reproduced density in photosynthetic reaction centre, previously considered disordered and missing from the crystals structure[152]. The possibility that serial data could regain at least some of this missing density was confirmed upon closer inspection of the serial density (Fig5.2). While the reclaimed density is limited to only four residues on each helix, it suggests secondary structure disordering and a more vertical trajectory which is less likely to interact with the SRII E-F helix. Our data does not preclude that this interaction may occur, as we are possibly catching one confirmation in preference over the other. Indeed, the activated state of the transducer is reported to weaken the binding between SRII and transducer, which may be associated with a conformational state that does not interact with the SRII EF-helix. The data shows that SRII-HtrII crystals with an improvement in diffraction quality or with increased source brilliance could probably resolved the structure to high resolution. This combined with greater redundancy in the dataset could likely reveal more structural features and permit time-resolved experiments at XFELs.

5.1.5 Paper IV: conclusion

In **Paper IV**, we show the viability of our new SRII-HtrII condition and crystal form to serial crystallography experiments. We show that with the addition of an appropriate substitute, SRII-HtrII can be crystallized without the need for purple membrane lipids. We successfully managed to collect a low-resolution dataset for SRII-HtrII by serial millisecond crystallography and solved the structure with a new space group to 2.1Å. The new solution had slightly less definition in the electron density but reveal four more residues on each TM helix of the transducer. This shows promise for retrieving for density at a higher resolution and for performing TRX experiments.

5.2 Paper V: SRII-HtrII signalling via TR-XSS

5.2.1 – Data collection

SRII and HtrII was expressed and purified as described in chapter 2. The sample was frozen and taken to ESRF-ID09. A 0.5 mm quartz capillary (Hampton research) was sliced at both ends and plastic (PTFE) tubing was attached onto either end by heat-shrink tubing. This capillary-tubing system was carefully mounted onto a goniometer and positioned at the X-ray and laser focal point. Sample was pumped back and forth past the sample position using a Nemesys pumping system. The protein sample was concentrated to ~20-60 mg/ml to improve the signal-to-noise ratio. The laser pulse was set at 450 nm, slightly off the absorption maxima at 498 nm, to improve sample penetration. 2 µs and 20 µs X-ray pulses for short (<6.3 µs) and long time points respectively. Nine time delays were logarithmically spaced apart, 2.5 µs, 6.3 µs, 20 µs, 63 µs, 200 µs, 630 µs, 2 ms, 6.3 ms and 20 ms. This allowed us to measure across three orders of magnitude appropriate for large structural shifts. The detector integrated 100 pumped probe pulses per image readout. This balanced requirements for reasonable signal in each image against the risk that anomalous peaks are measured during extended collection, while preventing detector saturation. Anomalous peaks can be introduced by bubbles in the capillary, a particular problem with the detergents used for membrane protein samples or cosmic rays. Collected images were azimuthally averaged into a 1-D curve and then averaged together. The absolute scattering was monitored for reduced protein scattering and sample was replaced when appropriate. Data was collected until sufficient averaging to reduce the curves noise to converge to a consistent scattering curve. To account for the laser heating the sample measurements with an IR pulse where used to simulate the heating effects. The protein signal was completely lost, reinforcing the conclusion that the difference effects where not protein specific. These heating curves where used to remove the heating effect from the scattering data.

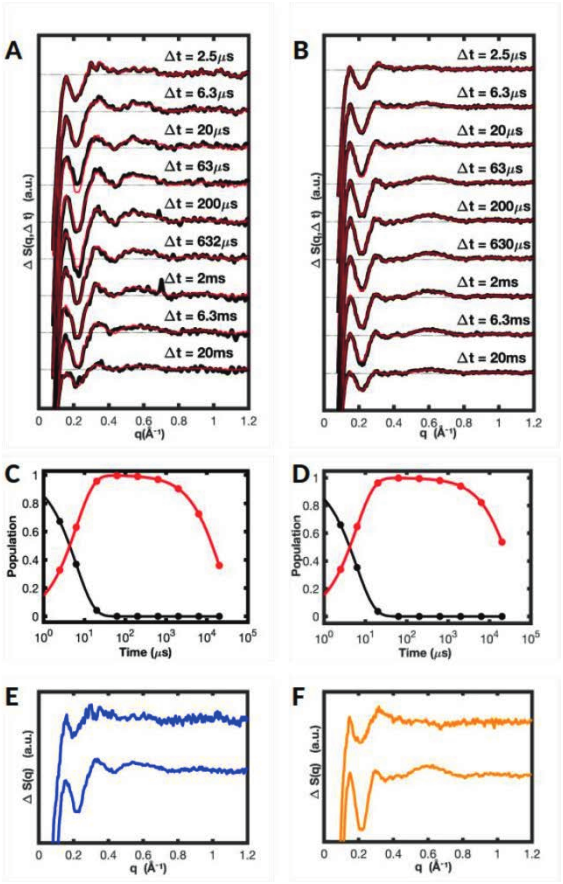

Figure 5.3, Difference WAXS curves and linear decomposition, a) Difference curves from SRII after activation b) Difference curves for SRII-HtrII after activation c) Relative populations for basis spectra over the time evolution SRII d) Relative populations for basis spectra over the time evolution SRII-HtrII e) Basis spectra calculated from linear decomposition of SRII f) Basis spectra calculated from linear decomposition of SRII-HtrII

5.2.2 Experimental difference curves

Experimental difference curves for SRII alone show an initial peak and depression at ~0.15Å^{-1} q and ~0.22Å^{-1} q, followed by a secondary peak between ~0.3-0.5Å^{-1} q and a final broad peak between ~0.45-0.75Å^{-1} q. These are visible throughout the time-points, with weakening signal in the longer

time points as sample leaves the sample spot. With the addition of the complex, similar features are observed in q. The initial low q peak (~0.15Å^{-1}) is higher and the depression is the same. The second peak becomes smaller shifting in q to~0.3Å^{-1}. This effectively flats the second peak. The final peak shift slightly in q to centre at 0.6Å^{-1}.

5.2.3 Data analysis and modelling

Data was subject to outlier rejection and reduced to a basic 1D-plot and the heat was removed. Linear decomposition reveals the rise and experimental clearance of a single intermediate. The curves for SRII only and transducer bound are remarkably similar. Both have a similar time constant, $\tau_1 \approx 6$ µs. The decay is the effect of experimental sample removal, while the small differences are the effect of the two different experimental setups. Linear decomposition shows that the addition of the transducer does appear to affect time constants for the structure of the early structural intermediate. This suggests that early structural changes are similar in SRII and SRII-HtrII. Furthermore, this fast time constant correlates well with other time constants for the early structural changes in microbial rhodopsins more generally. Also reflected in the basis spectra produced from the linear decomposition for SRII, TR-XSS shows close similarity to the bR basis spectra.

As in early bR studies[139], the basis spectra were used to model the intermediate structures. The extracted basis spectra for SRII and SRII-HtrII showed clear differences similar to those described for the difference curve series. Due to the stark similarities with bR basis spectra, the EF-helix and C helix were selected to interpolate. The nature of the EF movement was derived from a recent SMX structure published for bR at 1.725 ms[59], residues 141-173 were selected corresponding to residues 153-185. The C-helix transition was taken from **Paper III** in this thesis utilizing residues 71-81. Once interpolated onto the SRII structure, the extent of the excited state was modulated by an integer multiplier. The multiplier was then optimized via a simplex Nelder-Mead search algorithm. The resulting structural fits display the experimental difference features and fitted curves. shows the best fit

model for SRII where the overall shape shows good agreement. The protein regions at ~0.25-1.0Å^{-1} q show good agreement with the initial depression and the following two protein scattering peaks both have similar features in the theoretical scattering curves. The small difference between experimental and theoretical are likely caused by the modelling strategy and improvements in refinement method, a better description of the membrane will likely achieve a better fit. The SRII-HtrII theoretical fit also describes the major difference scattering features seen in the experimental data. The initial depression and subsequent peak appear better than SRII, the broadness in the third peak is again missed.

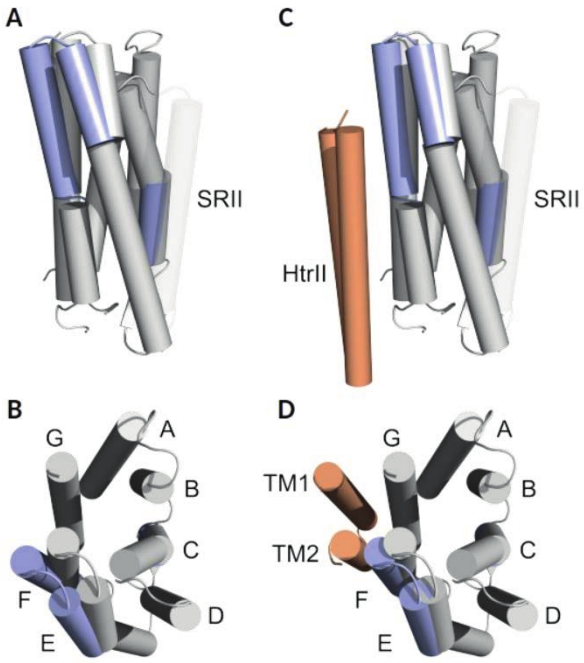

Figure 5.3, Modelled changes for the basis spectra, a) Imposed helical shift (blue) on the resting state structure of SRII (grey) b) Identical representation to (a) view perpendicular to the membrane c) Imposed helical shift (blue) on the resting state structure of SRII (grey) and HtrII (red) d) Identical representation to (c) view perpendicular to the

The best-fit models from only SRII show an 0.88 shift in the C-helix movement and a 0.58 movement in the EF helix. Therefore, the crystallographic movement is larger than seen in the scattering, which is surprising given the relative freedom that the solution scattering has to a crystal constrain protein. Upon binding the transducer, the EF helix movement was 0.31 for the movement. This is a 50% reduction in the EF-helix movement and means that the scatter 0.3-0.5$Å^{-1}$ is correlated to the movements in this helix. Similar observations were made in earlier bR TR-XSS experiments, where the earlier structural intermediate had a higher 0.3$Å^{-1}$ peak and modelled a larger movement in the EF-helix. That HtrII addition reduces the EF-helix movement strongly suggests that the transducer and helix TM2 interact upon activation.

5.2.4 Discussion

TR-XSS data record the scattering from an isomorphous solution sample the relatively low information content means that structural interpretation is based on modelling plausible intermediate. The scattering observed here correlates well with scattering observed for earlier rhodopsin TR-XSS studies, particularly bR[140,139]. The initial structural perturbations provided from recent TR-SMX studies on SRII and bR have produced highly plausible structural movements for SRII and SRII-HtrII. The EF helical movements has been observed in freeze trapped SRII[147] and in TR-SFX and TR-SMX studies on bR[59,56]. Modelling these structural changes produced a good fit. Signal transduction via large structural changes has been suggested to work through EF helices. These movements would likely interact with crystallographically unobserved domains on the TM helices[153]. Whether this looped region is functional is still an open question. Chimeric studies, removing either side and all of the EF-loop, showed cell swimming reversal still active. However, whether the remaining truncated region still undergoes a structural shift that could transmit this signal cannot be determined. Indeed, swimming motility from complete removal are reduced against wildtype[154]. Time-resolved FTIR measurements on early structural changes

suggest that hydrogen bonding close to the retinal directly transmits the signal to the transducer[145]. While crystallographic evidence is mixed, freeze trapped M-state structures with signal transmission through the hydrogen bonding network but also find an outward movement on the F-helix, in agreement with other measurements[37,75,155]. The helical movement is thought to rotate the transducer via interaction with the TM2 helix observed by freeze trapped M-state[74]. Fundamentally, these two mechanisms are not at odds with one another. An early signal transmission mediated via hydrogen bonds near the Schiff base followed by a structural signal in helical movements, thereby splitting the signal transmission into a two-step process, provides a very plausible complete mechanism for signal transduction.

6. Conclusions and future perspectives

6.1 Conclusions

This thesis has focused on the structural rearrangements in SRII and its cognate transducer HtrII. Ultrafast studies on bR complemented this and provided an understanding of the ultrafast movements that could likely be occurring in SRII.

In **Paper I**, we developed a new way of crystallizing SR II without the need for purple membrane lipids. We employ new crystallisation techniques developed in our lab to grow large numbers of crystals in LCP for serial crystallography and achieved high resolution diffraction at BioMAX.

In **Paper II**, we measure ultrafast structural changes in bR. This reveal the structural changes and related intermediates on a femtosecond time-scale that define isomerization.

In **Paper III**, using the crystallisation parameters developed in **Paper I** we measured and excited state structure for SR II by TR-SMX. The crystals diffracted to 2.1Å in the light and 2.5Å in the dark. The difference structure revealed that Thr204 plays a key role in limiting the movement on helix-G and lengthening the time of the intermediate states.

In **Paper IV**, we managed to grow microcrystals for SRII-HtrII without using purple membrane lipids through the addition of phytantriol. These crystals diffracted to low resolution during our SMX experiment but enough to collect a dataset. This data set revealed extra helical density caused by high redundancy serial data

Finally, in **Paper V** we measured the difference scattering from SRII and SRII-HtrII. We saw a strong difference signal similar to that from previous

measured bR. The addition of transducer causes a noticeable difference in the scattering curves. We modelled this difference to suggest that the transducer limits an outward EF-tilt upon activation. This provides evidence for a signalling role for the EF helix.

6.2 Future perspectives

Time-resolved structural biology has the ability to provide key insights into the structural changes during a protein's function. This provides an exciting possibility to map out protein dynamics and the amino acid configurations responsible for certain dynamic systems and regimes. The time-resolved field has taken a profound leap forward with the advent of XFELs, and this has only grown in recent years. This work has spilled back into XFEL experiments with data collection schemes that are not technically challenging to add to beamlines. Protein triggering scheme for non-light triggered proteins are taking steps forward and the next great challenge will be to bring time-resolved to the lay-structural biologist.

SRII has been well studied, particularly in comparison to bR. Here we provide new evidence, utilizing new X-ray techniques, that shed light on the structural intermediates in prokaryotic signalling. Furthermore, our results provide new evidence for the extended photocycles in SRII that is indicative of the known sensory rhodopsins. The new microcrystals for SRII-HtrII are an exciting development, as they provide the possibility for TR-SFX and TR-SMX studies of signal transduction through bound membrane proteins. This opens up possibilities to better understand prokaryotic signalling and explore a potential new drug target due to the prevalence of similar systems in microorganisms but not humans. Open questions about the exact nature of signal transfer remain, which will be considerably helped by further time-resolved studies.

8. Acknowledgements

When I came to Sweden 4 years ago I knew nothing except that I wanted to do a PhD. I had did not realize how lucky I had been to come to Lundberg. Considering the four years I have had, and the incredibly kind a generous people I have been fortunate enough to meet I realize the luck I have had.

Richard, I feel incredibly lucky to have been able to join your lab. When looking for a PhD position I came across someone who was interested in similar questions to me. It took us a while to work out how the other worked, but what I have learnt from you has been invaluable. Your fairness with your students and advocacy for them will always be something I will try to emulate.

Gisela, I really could not have wish for a better co-supervisor, your regular meetings have provided a much needed source of order. I will never forget the Hunt for the missing space group at SLS (C222...) or the ESRF beamtime where the difference curves showed some highly questionable results. Thank you for all of your support.

Daniel, we are both going to hell, I have had a one-way ticket for some time it's nice of you to join me. Ever since the optimistic but naive Daniel suddenly realize that it was week 2 of the PhD and he was responsible data processing at my first beamtime I have had a brother in WAXS arms...and in hell that gets messy. Seriously, you have been a constant source of fun and it's been needed. Anyway, your almost there Daniel, any day now you can start your PhD. :)

Giorgia, my crystallographic partner in crime. Having someone as enthusiastic as you join the SRII project was vital for me this last year. You were always optimistic; we went through the lows of BioMAX and the highs of SLS its been a crazy time. SRII-HtrII beckons, I look forward to thumbing a copy of Ortalani.et.al in nature someday soon.

Greger, you are the epitome of someone who is too respectable for me to know. Next time I need a chat about, are we living in a simulation or a science article about the mechanistic function of sleep... while writing my kappa... You have been a constant source of support over the years and I look forward to more esoteric conversations in future.

Cecilia W, Much ado about rhodopsins, of the rhodopsin people we were always ying and yang in style. But I always enjoyed the conversations that we had and theories we have developed, I fondling recognize the overanalyzing tendencies, its a fun club we have tee-shirts.

Per, Mr reliable, I should get you a cape with a spanner. Thank you for all the times that you looked after the cats, and assisted with beam-

times. Once that electric-field box is finally built I look forward to some pretty cool science.
Swagatha, constructing microspec, WAXS experiments, its been good to have someone to laugh when we fail and come up with new crazy ideas. The extrusion stuff looks really cool!!
Tinna, Thanks for everything! I am a chaotic mess at times and I am sorry you had to bear the brunt of it. Your support on the experiments was invaluable.
Petra B, Your help towards the end of my thesis when everything was getting chaotic, busy and stressful has been invaluable. Thank you.
Cecilia S, You have been a constant source of making a good day better, Japan was fun, very educational. Your skill as the LCP master is undisputed and your thesis looks great!!
Rebecka, Whenever I needed information about my personal life out there, you were there for me. You really provided support at the beginning of the PhD and it means a lot.
To the new CcO people, **Johanthan, Doris and Owens,** You guys seem super happy, I wish you all the best, PhD is a big adventure!! have fun.
Jenny H, I will miss those ESR meetings they were a lot of fun!! Apparently, we are supposed to organize a X-probe reunion, well I will be there if they do. I wish you and Emil all the best!
To the Westenhoff people, **Sebastian**, thanks for the lunch room conversations and letting me test sample at LCLS. The phytochrome result is really elegant! **Elin**, the saga continues! I have always enjoyed our chats, your questions are always thought provoking!!
Leocadie, Thanks for marking my work!!, I am not totally useless, sorry about the windows though!**Mattias,** It always nice to find a slightly dark sense of humor. **Weixao,** as a British person am I always drawn to a large cup of tea, thanks for all the chats. **Amke,** thanks for leading me your office, you get daniel back as well if you want :). **Andrea,** my fellow workaholic you have joined the darkside, I have enjoyed having you in the lab on late night. Don't let it consume you.
Gergely, thanks for putting up with my heinously trivial way of solving computational problems and me when I missing the obvious. Viktor, Congratulations on the little one and good luck with the Science. Maja it's been great to get to know you I hope that hanna enjoyed crystallizing and that your PhD has more of a theme.
To the **Bjormann** group, **Bjorn** thanks for the conversations and suggestions and considering what how NMR could help the project we got too busy in the end but its appreciated. **Emeilie** and **Darius,** thanks for all the help with the Äktas and being very patient with me when I am disorganized. Lisa thanks for adopting the tomato plant and helping the when we needed compontent cells. **Johannes and Ylber**, when I do attend beer club our conversations are always interesting.

Irena, its always good to see you! **Ashish, Damasus and Jens**, I wish you all the best.
Johanna, thanks for the good EM talk, may you never be tempted to the dark world of SPR.
Davide and the rest of the Höög group, **Jacob, Katarina and Lisa**, good luck with the EM you guys have a really nice group I wish you all the best
To the Kristina crowd, Florian I will miss our occasional political chats, **Jessica**, I still don't quite understand your project but it's always fun to chat. **Kristina,** thank you for providing me good suggestions when needed.
Arwen, 6 years ago you lectured to a bunch of students, about XFELs and Time-resolved serial crystallography. Its exactly that sort of dangerous enthusiasm that gets people sent to Sweden. Thank you.

Torsten and **Guneborg**, thank you for welcoming me into the family, I look forward to trips back to falun. It been a great way relax.

To my family, you may have grown suspicious over the years as I slowly migrated further and further away. Some of you were surprised when I told you I was moving to Sweden to do a PhD, liberal hippy professor leading me down a path of tofu and veganism. I have always valued your support over the years and while fairly stubborn. I love all of you and unfortunately for you I am going to be a lot closer.

Astrid, without you this thesis would have never been written in so many different way. You have been my constant support, all the way down until the final thesis handin. I love you and cannot wait to get married. Lets go and start another crazy adventure.

9. Bibliography

1 Friel, C. T., Smith, D. A., Vendruscolo, M., Gsponer, J. & Radford, S. E. The mechanism of folding of Im7 reveals competition between functional and kinetic evolutionary constraints. *Nat Struct Mol Biol* **16**, 318-324, doi:10.1038/nsmb.1562 (2009).

2 Anfinsen, C. B. Principles that Govern the Folding of Protein Chains. doi:10.1126/science.181.4096.223 (1973).

3 Bae, E. & Phillips, G. N. Structures and Analysis of Highly Homologous Psychrophilic, Mesophilic, and Thermophilic Adenylate Kinases. *J. Biol. Chem.* **279**, 28202-28208, doi:10.1074/jbc.M401865200 (2004).

4 Mitchell, P. Coupling of Phosphorylation to Electron and Hydrogen Transfer by a Chemi-Osmotic type of Mechanism. *Nature* **191**, 144-148, doi:10.1038/191144a0 (1961).

5 Harayama, T. & Riezman, H. Understanding the diversity of membrane lipid composition. *Nature Reviews Molecular Cell Biology* **19**, 281-296, doi:10.1038/nrm.2017.138 (2018).

6 Sezgin, E., Levental, I., Mayor, S. & Eggeling, C. The mystery of membrane organization: composition, regulation and roles of lipid rafts. *Nature Reviews Molecular Cell Biology* **18**, 361-374, doi:10.1038/nrm.2017.16 (2017).

7 Trubelja, A. & Bao, G. Molecular mechanisms of mechanosensing and mechanotransduction in living cells. *Extreme Mechanics Letters* **20**, 91-98, doi:10.1016/j.eml.2018.01.011 (2018).

8 Kechagia, J. Z., Ivaska, J. & Roca-Cusachs, P. Integrins as biomechanical sensors of the microenvironment. *Nature Reviews Molecular Cell Biology* **20**, 457-473, doi:10.1038/s41580-019-0134-2 (2019).

9 Cox, C. D., Bavi, N. & Martinac, B. Bacterial Mechanosensors. *Annual Review of Physiology* **80**, 71-93, doi:10.1146/annurev-physiol-021317-121351 (2018).

10 Yu, F. H. & Catterall, W. A. The VGL-Chanome: A Protein Superfamily Specialized for Electrical Signaling and Ionic

Homeostasis. *Sci. Signal.* **2004**, re15, doi:10.1126/stke.2532004re15 (2004).
11 Kaczmarek, L. K. Non-conducting functions of voltage-gated ion channels. *Nat Rev Neurosci* **7**, 761-771, doi:10.1038/nrn1988 (2006).
12 Long, S. B., Tao, X., Campbell, E. B. & MacKinnon, R. Atomic structure of a voltage-dependent K + channel in a lipid membrane-like environment. *Nature* **450**, 376-382, doi:doi:10.1038/nature06265 (2019).
13 Kawate, T., Michel, J. C., Birdsong, W. T. & Gouaux, E. Crystal structure of the ATP-gated P2X 4 ion channel in the closed state. *Nature* **460**, 592-598, doi:doi:10.1038/nature08198 (2009).
14 Steinbacher, S., Bass, R., Strop, P. & Rees, D. C. in *Current Topics in Membranes* Vol. 58 1-24 (Academic Press, 2007).
15 Rasmussen, S. G. F. *et al.* Crystal structure of the β 2 adrenergic receptor–Gs protein complex. *Nature* **477**, 549-555, doi:doi:10.1038/nature10361 (2011).
16 Varma, N. *et al.* Crystal structure of jumping spider rhodopsin-1 as a light sensitive GPCR. doi:10.1073/pnas.1902192116 (2019).
17 Ortells, M. O. & Lunt, G. G. Evolutionary history of the ligand-gated ion-channel superfamily of receptors. *Trends in Neurosciences* **18**, 121-127, doi:10.1016/0166-2236(95)93887-4 (1995).
18 Collingridge, G. L., Olsen, R. W., Peters, J. & Spedding, M. A nomenclature for ligand-gated ion channels. *Neuropharmacology* **56**, 2-5, doi:10.1016/j.neuropharm.2008.06.063 (2009).
19 Brejc, K. a. *et al.* Crystal structure of an ACh-binding protein reveals the ligand-binding domain of nicotinic receptors. *Nature* **411**, 269-276, doi:10.1038/35077011 (2001).
20 Hassaine, G. *et al.* X-ray structure of the mouse serotonin 5-HT₃ receptor. *Nature* **512**, 276-281, doi:10.1038/nature13552 (2014).
21 Zhu, S. *et al.* Structure of a human synaptic GABA A receptor. *Nature* **559**, 67-72, doi:10.1038/s41586-018-0255-3 (2018).

22 Traynelis, S. F. *et al.* Glutamate Receptor Ion Channels: Structure, Regulation, and Function. *Pharmacol Rev* **62**, 405-496, doi:10.1124/pr.109.002451 (2010).
23 Hattori, M. & Gouaux, E. Molecular mechanism of ATP binding and ion channel activation in P2X receptors. *Nature* **485**, 207-212, doi:10.1038/nature11010 (2012).
24 Schmid, R. & Evans, R. J. ATP-Gated P2X Receptor Channels: Molecular Insights into Functional Roles. *Annual Review of Physiology* **81**, 43-62, doi:10.1146/annurev-physiol-020518-114259 (2019).
25 Lemmon, M. A. & Schlessinger, J. Cell Signaling by Receptor Tyrosine Kinases. *Cell* **141**, 1117-1134, doi:10.1016/j.cell.2010.06.011 (2010).
26 Takahashi, T., Mochizuki, Y., Kamo, N. & Kobatake, Y. Evidence that the long-lifetime photointermediate of s-rhodopsin is a receptor for negative phototaxis in halobacterium halobium. *Biochemical and Biophysical Research Communications* **127**, 99-105, doi:10.1016/S0006-291X(85)80131-5 (1985).
27 Spudich, E. N. S. S. A. S. D. M. D. J. L. Properties of a second sensory receptor protein in Halobacterium halobium phototaxis - Spudich - 1986 - Proteins: Structure, Function, and Bioinformatics - Wiley Online Library. doi:10.1002/prot.340010306 (1986).
28 Vogeley, L. *et al.* Anabaena Sensory Rhodopsin: A Photochromic Color Sensor at 2.0 Å. doi:10.1126/science.1103943 (2004).
29 Pushkarev, A. *et al.* A distinct abundant group of microbial rhodopsins discovered using functional metagenomics. *Nature* **558**, 595-599, doi:doi:10.1038/s41586-018-0225-9 (2018).
30 Shihoya, W. *et al.* Crystal structure of heliorhodopsin. *Nature* **574**, 132-136, doi:doi:10.1038/s41586-019-1604-6 (2019).
31 Chizhov, I. *et al.* The Photophobic Receptor from Natronobacterium pharaonis: Temperature and pH Dependencies of the Photocycle of Sensory Rhodopsin II. *Biophysical Journal* **75**, 999-1009, doi:10.1016/S0006-3495(98)77588-5 (1998).
32 Váró, G. *et al.* Photocycle of halorhodopsin from Halobacterium salinarium. *Biophysical Journal* **68**, 2062-2072 (1995).

33 Lozier, R. H., Bogomolni, R. A. & Stoeckenius, W. Bacteriorhodopsin: a light-driven proton pump in Halobacterium Halobium. *Biophysical Journal* **15**, 955-962, doi:10.1016/S0006-3495(75)85875-9 (1975).

34 Hamm, P. *et al.* Femtosecond spectroscopy of the photoisomerisation of the protonated Schiff base of all-trans retinal. *Chemical Physics Letters* **263**, 613-621, doi:10.1016/S0009-2614(96)01269-9 (1996).

35 Diller, R. *et al.* The trans-cis isomerization reaction dynamics in sensory rhodopsin II by femtosecond time-resolved midinfrared spectroscopy: Chromophore and protein dynamics. *Biopolymers* **82**, 358-362, doi:10.1002/bip.20475 (2006).

36 Ulrich Haupts, Jörg Tittor, a. & Oesterhelt, D. CLOSING IN ON BACTERIORHODOPSIN: Progress in Understanding the Molecule. *http://dx.doi.org.ezproxy.ub.gu.se/10.1146/annurev.biophys.28.1.367*, doi:10.1146/annurev.biophys.28.1.367 (2003).

37 Wegener, A.-A., Chizhov, I., Engelhard, M. & Steinhoff, H.-J. Time-resolved detection of transient movement of helix F in spin-labelled pharaonis sensory rhodopsin II11Edited by W. Baumeister. *Journal of Molecular Biology* **301**, 881-891, doi:10.1006/jmbi.2000.4008 (2000).

38 Sudo, Y., Iwamoto, M., Shimono, K., Sumi, M. & Kamo, N. Photo-induced proton transport of pharaonis phoborhodopsin (sensory rhodopsin II) is ceased by association with the transducer. *Biophys J* **80**, 916-922, doi:10.1016/s0006-3495(01)76070-5 (2001).

39 Shibukawa, A. *et al.* Photochemical Characterization of a New Heliorhodopsin from the Gram-Negative Eubacterium Bellilinea caldifistulae (BcHeR) and Comparison with Heliorhodopsin-48C12. *Biochemistry* **58**, 2934-2943, doi:10.1021/acs.biochem.9b00257 (2019).

40 Schobert, B. & Lanyi, J. K. Halorhodopsin is a light-driven chloride pump. *J. Biol. Chem.* **257**, 10306-10313 (1982).

41 Oesterhelt, D., Hegemann, P. & Tittor, J. The photocycle of the chloride pump halorhodopsin. II: Quantum yields and a kinetic model. *EMBO J* **4**, 2351-2356 (1985).

42 Kolbe, M., Besir, H., Essen, L.-O. & Oesterhelt, D. Structure of the Light-Driven Chloride Pump Halorhodopsin at 1.8 Å Resolution. *Science* **288**, 1390-1396, doi:10.1126/science.288.5470.1390 (2000).

43 Andersson, M., Vincent, J., Spoel, D. v. d., Davidsson, J. & Neutze, R. A Proposed Time-Resolved X-Ray Scattering Approach to Track Local and Global Conformational Changes in Membrane Transport Proteins. *Structure* **16**, 21-28, doi:10.1016/j.str.2007.10.016 (2008).

44 Kouyama, T., Kawaguchi, H., Nakanishi, T., Kubo, H. & Murakami, M. Crystal Structures of the L1, L2, N, and O States of pharaonis Halorhodopsin. *Biophysical Journal* **108**, 2680-2690, doi:10.1016/j.bpj.2015.04.027 (2015).

45 Sasaki, J. *et al.* Conversion of bacteriorhodopsin into a chloride ion pump. *Science* **269**, 73-75, doi:10.1126/science.7604281 (1995).

46 Nagel, G. *et al.* Channelrhodopsin-2, a directly light-gated cation-selective membrane channel. *PNAS* **100**, 13940-13945, doi:10.1073/pnas.1936192100 (2003).

47 Nagel, G. *et al.* Light Activation of Channelrhodopsin-2 in Excitable Cells of Caenorhabditis elegans Triggers Rapid Behavioral Responses. *Current Biology* **15**, 2279-2284, doi:10.1016/j.cub.2005.11.032 (2005).

48 Fenno, L., Yizhar, O. & Deisseroth, K. The Development and Application of Optogenetics. *Annual Review of Neuroscience* **34**, 389-412, doi:10.1146/annurev-neuro-061010-113817 (2011).

49 Volkov, O. *et al.* Structural insights into ion conduction by channelrhodopsin 2. *Science* **358**, doi:10.1126/science.aan8862 (2017).

50 Lórenz-Fonfría, V. A. *et al.* Temporal evolution of helix hydration in a light-gated ion channel correlates with ion conductance. doi:10.1073/pnas.1511462112 (2015).

51 Henderson, R. & Unwin, P. N. T. Three-dimensional model of purple membrane obtained by electron microscopy. *Nature* **257**, 28-32, doi:10.1038/257028a0 (1975).

52 Pebay-Peyroula, E., Rummel, G., Rosenbusch, J. P. & Landau, E. M. X-ray Structure of Bacteriorhodopsin at 2.5 Angstroms

from Microcrystals Grown in Lipidic Cubic Phases. *Science* **277**, 1676-1681, doi:10.1126/science.277.5332.1676 (1997).

53 Kobayashi, T., Saito, T. & Ohtani, H. Real-time spectroscopy of transition states in bacteriorhodopsin during retinal isomerization. *Nature* **414**, 531-534, doi:doi:10.1038/35107042 (2019).

54 Schenkl, S., Mourik, F. v., Zwan, G. v. d., Haacke, S. & Chergui, M. Probing the Ultrafast Charge Translocation of Photoexcited Retinal in Bacteriorhodopsin. doi:10.1126/science.1111482 (2005).

55 Royant, A. *et al.* Helix deformation is coupled to vectorial proton transport in the photocycle of bacteriorhodopsin. *Nature* **406**, 645-648, doi:10.1038/35020599 (2000).

56 Nango, E. *et al.* A three-dimensional movie of structural changes in bacteriorhodopsin. *Science* **354**, 1552-1557, doi:10.1126/science.aah3497 (2016).

57 Sass, H. J. *et al.* Structural alterations for proton translocation in the M state of wild-type bacteriorhodopsin. *Nature* **406**, 649-653, doi:10.1038/35020607 (2000).

58 Richter, H.-T., Brown, L. S., Needleman, R. & Lanyi, J. K. A Linkage of the pKa's of asp-85 and glu-204 Forms Part of the Reprotonation Switch of Bacteriorhodopsin. *Biochemistry* **35**, 4054-4062, doi:10.1021/bi952883q (1996).

59 Weinert, T. *et al.* Proton uptake mechanism in bacteriorhodopsin captured by serial synchrotron crystallography. *Science* **365**, 61-65, doi:10.1126/science.aaw8634 (2019).

60 Olson, K. D. & Spudich, J. L. Removal of the transducer protein from sensory rhodopsin I exposes sites of proton release and uptake during the receptor photocycle. *Biophysical Journal* **65**, 2578-2585, doi:10.1016/S0006-3495(93)81295-5 (1993).

61 Bogomolni, R. A. & Spudich, J. L. The photochemical reactions of bacterial sensory rhodopsin-I. Flash photolysis study in the one microsecond to eight second time window. *Biophys J* **52**, 1071-1075, doi:10.1016/s0006-3495(87)83301-5 (1987).

62 Hippler-Mreyen, S. *et al.* Probing the Sensory Rhodopsin II Binding Domain of its Cognate Transducer by Calorimetry and Electrophysiology. *Journal of Molecular Biology* **330**, 1203-1213, doi:10.1016/S0022-2836(03)00656-9 (2003).

63 Orekhov, P. *et al.* Sensory Rhodopsin I and Sensory Rhodopsin II Form Trimers of Dimers in Complex with their Cognate Transducers. *Photochemistry and Photobiology* **93**, 796-804, doi:10.1111/php.12763 (2017).

64 Gushchin, I. *et al.* Mechanism of transmembrane signaling by sensor histidine kinases. doi:10.1126/science.aah6345 (2017).

65 Welch, M., Oosawa, K., Aizawa, S. & Eisenbach, M. Phosphorylation-dependent binding of a signal molecule to the flagellar switch of bacteria. doi:10.1073/pnas.90.19.8787 (1993).

66 Barak, R. & Eisenbach, M. Correlation between phosphorylation of the chemotaxis protein CheY and its activity at the flagellar motor. doi:10.1021/bi00121a034 (2002).

67 Schmies, G., Engelhard, M., Wood, P. G., Nagel, G. & Bamberg, E. Electrophysiological characterization of specific interactions between bacterial sensory rhodopsins and their transducers. *PNAS* **98**, 1555-1559, doi:10.1073/pnas.98.4.1555 (2001).

68 Sudo, Y. & Spudich, J. L. Three strategically placed hydrogen-bonding residues convert a proton pump into a sensory receptor. doi:10.1073/pnas.0607467103 (2006).

69 Iwamoto, M., Shimono, K., Sumi, M. & Kamo, N. Positioning proton-donating residues to the Schiff-base accelerates the M-decay of pharaonis phoborhodopsin expressed in Escherichia coli. *Biophys. Chem.* **79**, 187-192, doi:10.1016/s0301-4622(99)00054-x (1999).

70 Miyazaki, M., Hirayama, J., Hayakawa, M. & Kamo, N. Flash photolysis study on pharaonis phoborhodopsin from a haloalkaliphilic bacterium (Natronobacterium pharaonis). *Biochimica et Biophysica Acta (BBA) - Bioenergetics* **1140**, 22-29, doi:10.1016/0005-2728(92)90015-T (1992).

71 Takao, K.-i., Kikukawa, T., Araiso, T. & Kamo, N. Azide accelerates the decay of M-intermediate of pharaonis phoborhodopsin. *Biophys. Chem.* **73**, 145-153, doi:10.1016/S0301-4622(98)00156-2 (1998).

72 Ito, M. *et al.* Steric Constraint in the Primary Photoproduct of Sensory Rhodopsin II Is a Prerequisite for Light-Signal Transfer to HtrII. *Biochemistry* **47**, 6208-6215, doi:10.1021/bi8003507 (2008).

73 Sudo, Y., Furutani, Y., Shimono, K., Kamo, N. & Kandori, H. Hydrogen bonding alteration of Thr-204 in the complex between pharaonis phoborhodopsin and its transducer protein. *Biochemistry* **42**, 14166-14172, doi:10.1021/bi035678g (2003).
74 Moukhametzianov, R. *et al.* Development of the signal in sensory rhodopsin and its transfer to the cognate transducer. *Nature* **440**, 115-119, doi:doi:10.1038/nature04520 (2006).
75 Gordeliy, V. I. *et al.* Molecular basis of transmembrane signalling by sensory rhodopsin II–transducer complex. *Nature* **419**, 484-487, doi:10.1038/nature01109 (2002).
76 Etzkorn, M. *et al.* Complex Formation and Light Activation in Membrane-Embedded Sensory Rhodopsin II as Seen by Solid-State NMR Spectroscopy. *Structure* **18**, 293-300, doi:10.1016/j.str.2010.01.011 (2010).
77 Sudo, Y., Yamabi, M., Iwamoto, M., Shimono, K. & Kamo, N. Interaction of Natronobacterium pharaonis Phoborhodopsin (Sensory Rhodopsin II) with its Cognate Transducer Probed by Increase in the Thermal Stability¶. *Photochemistry and Photobiology* **78**, 511-516, doi:10.1562/0031-8655(2003)0780511IONPPS2.0.CO2 (2003).
78 Wegener, A.-A., Klare, J. P., Engelhard, M. & Steinhoff, H.-J. Structural insights into the early steps of receptor—transducer signal transfer in archaeal phototaxis. *EMBO J* **20**, 5312-5319, doi:10.1093/emboj/20.19.5312 (2001).
79 Yang, C.-S. & Spudich, J. L. Light-Induced Structural Changes Occur in the Transmembrane Helices of the Natronobacterium pharaonis HtrII Transducer. *Biochemistry* **40**, 14207-14214, doi:10.1021/bi010985c (2001).
80 Inoue, K., Sasaki, J., Morisaki, M., Tokunaga, F. & Terazima, M. Time-Resolved Detection of Sensory Rhodopsin II-Transducer Interaction. *Biophysical Journal* **87**, 2587-2597, doi:10.1529/biophysj.104.043521 (2004).
81 Ishchenko, A. *et al.* New Insights on Signal Propagation by Sensory Rhodopsin II/Transducer Complex. *Scientific Reports* **7**, 41811, doi:10.1038/srep41811 (2017).
82 Yang, C.-S., Sineshchekov, O., Spudich, E. N. & Spudich, J. L. The Cytoplasmic Membrane-proximal Domain of the HtrII Transducer Interacts with the E-F Loop of Photoactivated

Natronomonas pharaonis Sensory Rhodopsin II. *J. Biol. Chem.* **279**, 42970-42976, doi:10.1074/jbc.M406504200 (2004).

83 Nishikata, K., Fuchigami, S., Ikeguchi, M. & Kidera, A. Molecular modeling of the HAMP domain of sensory rhodopsin II transducer from Natronomonas pharaonis. *Biophysics* **6**, 27-36, doi:10.2142/biophysics.6.27 (2010).

84 Luecke, H., Schobert, B., Lanyi, J. K., Spudich, E. N. & Spudich, J. L. Crystal Structure of Sensory Rhodopsin II at 2.4 Angstroms: Insights into Color Tuning and Transducer Interaction. *Science* **293**, 1499-1503, doi:10.1126/science.1062977 (2001).

85 Privé, G. G. Detergents for the stabilization and crystallization of membrane proteins. *Methods* **41**, 388-397, doi:10.1016/j.ymeth.2007.01.007 (2007).

86 Schuler, M. A., Denisov, I. G. & Sligar, S. G. Nanodiscs as a new tool to examine lipid-protein interactions. *Methods Mol Biol* **974**, 415-433, doi:10.1007/978-1-62703-275-9_18 (2013).

87 Laemmli, U. K. Cleavage of Structural Proteins during the Assembly of the Head of Bacteriophage T4. *Nature* **227**, 680-685, doi:10.1038/227680a0 (1970).

88 Hohenfeld, I. P., Wegener, A. A. & Engelhard, M. Purification of histidine tagged bacteriorhodopsin, pharaonis halorhodopsin and pharaonis sensory rhodopsin II functionally expressed in Escherichia coli. *FEBS Letters* **442**, 198-202, doi:10.1016/S0014-5793(98)01659-7 (1999).

89 Kazumi Shimono, M. I., Masato Sumi, Naoki Kamo. Functional expression of pharaonis phoborhodopsin in Eschericha coli. *FEBS Letters* **volume 420**, doi:DOI: 10.1016/s0014-5793(97)01487-7 (1997).

90 Klare, J. P. *et al.* Effects of solubilization on the structure and function of the sensory rhodopsin II/transducer complex. *J Mol Biol* **356**, 1207-1221, doi:10.1016/j.jmb.2005.12.015 (2006).

91 Bragg, W. L. The Structure of Silicates 1. *Nature*.

92 Armstrong, H. E. Poor Common Salt! *Nature* **120**, 478-478, doi:10.1038/120478b0 (1927).

93 Newstead, S., Ferrandon, S. & Iwata, S. Rationalizing α-helical membrane protein crystallization. *Protein Science* **17**, 466-472, doi:10.1110/ps.073263108 (2008).

94 Caffrey, M. A comprehensive review of the lipid cubic phase or in meso method for crystallizing membrane and soluble proteins and complexes. *Acta Cryst F* **71**, 3-18, doi:10.1107/S2053230X14026843 (2015).
95 Dods, R. *et al.* From Macrocrystals to Microcrystals: A Strategy for Membrane Protein Serial Crystallography. *Structure* **25**, 1461-1468.e1462, doi:10.1016/j.str.2017.07.002 (2017).
96 Lee, D. B. *et al.* Supersaturation-controlled microcrystallization and visualization analysis for serial femtosecond crystallography. *Scientific Reports* **8**, 1-10, doi:doi:10.1038/s41598-018-20899-9 (2018).
97 Kupitz, C. *et al.* in *Philos Trans R Soc Lond B Biol Sci* Vol. 369 (2014).
98 Royant, A. *et al.* X-ray structure of sensory rhodopsin II at 2.1-Å resolution. *PNAS* **98**, 10131-10136, doi:10.1073/pnas.181203898 (2001).
99 Andersson, R. *et al.* Serial femtosecond crystallography structure of cytochrome c oxidase at room temperature. *Scientific Reports* **7**, 1-9, doi:10.1038/s41598-017-04817-z (2017).
100 The Nobel Prize in Physics 1914. (2019).
101 Meents, A. *et al.* Pink-beam serial crystallography. *Nature Communications* **8**, 1-12, doi:doi:10.1038/s41467-017-01417-3 (2017).
102 Kabsch, W. in *Acta Crystallogr D Biol Crystallogr* Vol. 66 125-132 (2010).
103 Duisenberg, A. J. M. & IUCr. Indexing in single-crystal diffractometry with an obstinate list of reflections. *Journal of Applied Crystallography* **25**, 92-96, doi:doi:10.1107/S0021889891010634 (1992).
104 Gevorkov, Y. *et al.* XGANDALF - extended gradient descent algorithm for lattice finding. *Acta Crystallogr A Found Adv* **75**, 694-704, doi:10.1107/s2053273319010593 (2019).
105 White, T. A. *et al.* CrystFEL: a software suite for snapshot serial crystallography. *Journal of Applied Crystallography* **45**, 335-341, doi:10.1107/S0021889812002312 (2012).

106 Emsley, P. & Cowtan, K. Coot: model-building tools for molecular graphics. *Acta Cryst D* **60**, 2126-2132, doi:10.1107/S0907444904019158 (2004).
107 Garman, E. F., Owen, R. L. & IUCr. Cryocooling and radiation damage in macromolecular crystallography. *Acta Crystallographica Section D: Biological Crystallography* **62**, 32-47, doi:doi:10.1107/S0907444905034207 (2005).
108 Davy, B. *et al.* Reducing sample consumption for serial crystallography using acoustic drop ejection. *J Synchrotron Rad* **26**, 1820-1825, doi:10.1107/S1600577519009329 (2019).
109 Nass, K. *et al.* Indications of radiation damage in ferredoxin microcrystals using high-intensity X-FEL beams. *J Synchrotron Rad* **22**, 225-238, doi:10.1107/S1600577515002349 (2015).
110 Coquelle, N. *et al.* Raster-scanning serial protein crystallography using micro- and nano-focused synchrotron beams. *Acta Cryst D* **71**, 1184-1196, doi:10.1107/S1399004715004514 (2015).
111 Boehr, D. D., McElheny, D., Dyson, H. J. & Wright, P. E. The Dynamic Energy Landscape of Dihydrofolate Reductase Catalysis. *Science* **313**, 1638-1642, doi:10.1126/science.1130258 (2006).
112 Holton, J. M. & Frankel, K. A. in *Acta Crystallogr D Biol Crystallogr* Vol. 66 393-408 (2010).
113 Doscher, M. S. & Richards, F. M. The Activity of an Enzyme in the Crystalline State: Ribonuclease S. *J. Biol. Chem.* **238**, 2399-2406 (1963).
114 Scheidig, A. J. *et al.* Time-resolved crystallography on H-ras p21. *Philosophical Transactions of the Royal Society of London. Series A: Physical and Engineering Sciences* **340**, 263-272, doi:10.1098/rsta.1992.0065 (1992).
115 Olmos, J. L. *et al.* Enzyme intermediates captured "on the fly" by mix-and-inject serial crystallography. *Bmc Biol* **16**, doi:ARTN 59
10.1186/s12915-018-0524-5 (2018).
116 Mehrabi, P. *et al.* Liquid application method for time-resolved analyses by serial synchrotron crystallography. *Nature Methods* **16**, 979-982, doi:10.1038/s41592-019-0553-1 (2019).
117 Hekstra, D. R. *et al.* Electric-field-stimulated protein mechanics. *Nature* **540**, 400-405, doi:10.1038/nature20571 (2016).

118 Suga, M. *et al.* Light-induced structural changes and the site of O=O bond formation in PSII caught by XFEL. *Nature* **543**, 131-135, doi:10.1038/nature21400 (2017).
119 Genick, U. K. *et al.* Structure of a Protein Photocycle Intermediate by Millisecond Time-Resolved Crystallography. *Science* **275**, 1471-1475, doi:10.1126/science.275.5305.1471 (1997).
120 Srajer, V. *et al.* Photolysis of the Carbon Monoxide Complex of Myoglobin: Nanosecond Time-Resolved Crystallography. *Science* **274**, 1726-1729, doi:10.1126/science.274.5293.1726 (1996).
121 Schotte, F. *et al.* Watching a Protein as it Functions with 150-ps Time-Resolved X-ray Crystallography. *Science* **300**, 1944-1947, doi:10.1126/science.1078797 (2003).
122 Rajagopal, S. *et al.* A Structural Pathway for Signaling in the E46Q Mutant of Photoactive Yellow Protein. *Structure* **13**, 55-63, doi:10.1016/j.str.2004.10.016 (2005).
123 Ihee, H. *et al.* Visualizing reaction pathways in photoactive yellow protein from nanoseconds to seconds. *Proc Natl Acad Sci U S A* **102**, 7145-7150, doi:10.1073/pnas.0409035102 (2005).
124 Wöhri, A. B. *et al.* Light-Induced Structural Changes in a Photosynthetic Reaction Center Caught by Laue Diffraction. *Science* **328**, 630-633, doi:10.1126/science.1186159 (2010).
125 Neutze, R., Wouts, R., van der Spoel, D., Weckert, E. & Hajdu, J. Potential for biomolecular imaging with femtosecond X-ray pulses. *Nature* **406**, 752-757, doi:10.1038/35021099 (2000).
126 Tenboer, J. *et al.* Time-resolved serial crystallography captures high-resolution intermediates of photoactive yellow protein. *Science* **346**, 1242-1246, doi:10.1126/science.1259357 (2014).
127 Barends, T. R. M. *et al.* Direct observation of ultrafast collective motions in CO myoglobin upon ligand dissociation. *Science* **350**, 445-450, doi:10.1126/science.aac5492 (2015).
128 Nogly, P. *et al.* Retinal isomerization in bacteriorhodopsin captured by a femtosecond x-ray laser. *Science* **361**, eaat0094, doi:10.1126/science.aat0094 (2018).
129 Kupitz, C. *et al.* Serial time-resolved crystallography of photosystem II using a femtosecond X-ray laser. *Nature* **513**, 261-265, doi:10.1038/nature13453 (2014).

130 Suga, M. *et al.* An oxyl/oxo mechanism for oxygen-oxygen coupling in PSII revealed by an x-ray free-electron laser. *Science* **366**, 334-338, doi:10.1126/science.aax6998 (2019).
131 Tosha, T. *et al.* Capturing an initial intermediate during the P450nor enzymatic reaction using time-resolved XFEL crystallography and caged-substrate. *Nat Commun* **8**, 1-9, doi:10.1038/s41467-017-01702-1 (2017).
132 Cammarata, M. *et al.* Tracking the structural dynamics of proteins in solution using time-resolved wide-angle X-ray scattering. *Nature methods* **5**, 881-886, doi:10.1038/nmeth.1255 (2008).
133 Franke, D. *et al.* ATSAS 2.8: a comprehensive data analysis suite for small-angle scattering from macromolecular solutions. *Journal of Applied Crystallography* **50**, 1212-1225, doi:doi:10.1107/S1600576717007786 (2017).
134 Björling, A. *et al.* Structural photoactivation of a full-length bacterial phytochrome. doi:10.1126/sciadv.1600920 (2016).
135 Berntsson, O. *et al.* Sequential conformational transitions and α-helical supercoiling regulate a sensor histidine kinase. *Nature Communications* **8**, 1-8, doi:doi:10.1038/s41467-017-00300-5 (2017).
136 Nelder, J. A., Mead, R. & National Vegetable Research Station, W., Warwick. A Simplex Method for Function Minimization. *The Computer Journal* **7**, 308-313, doi:10.1093/comjnl/7.4.308 (1965).
137 Mertens, H. D. T. & Svergun, D. I. Structural characterization of proteins and complexes using small-angle X-ray solution scattering. *Journal of Structural Biology* **172**, 128-141, doi:10.1016/j.jsb.2010.06.012 (2010).
138 Cho, H. S. *et al.* Protein structural dynamics in solution unveiled via 100-ps time-resolved x-ray scattering. *PNAS* **107**, 7281-7286, doi:10.1073/pnas.1002951107 (2010).
139 Andersson, M. *et al.* Structural Dynamics of Light-Driven Proton Pumps. *Structure* **17**, 1265-1275, doi:10.1016/j.str.2009.07.007 (2009).
140 Malmerberg, E. *et al.* Time-Resolved WAXS Reveals Accelerated Conformational Changes in Iodoretinal-Substituted

Proteorhodopsin. *Biophysical Journal* **101**, 1345-1353, doi:10.1016/j.bpj.2011.07.050 (2011).
141 Arnlund, D. *et al.* Visualizing a protein quake with time resolved X-ray scattering at a free electron laser. *Nature methods* **11**, 923-926, doi:10.1038/nmeth.3067 (2014).
142 Brändén, G. *et al.* Coherent diffractive imaging of microtubules using an X-ray laser. *Nat Commun* **10**, 1-9, doi:10.1038/s41467-019-10448-x (2019).
143 Weierstall, U. *et al.* Lipidic cubic phase injector facilitates membrane protein serial femtosecond crystallography. *Nat Commun* **5**, 1-6, doi:10.1038/ncomms4309 (2014).
144 Hayashi, S. *et al.* Structural Determinants of Spectral Tuning in Retinal ProteinsBacteriorhodopsin vs Sensory Rhodopsin II [#]. *The Journal of Physical Chemistry B* **105**, 10124-10131, doi:10.1021/jp011362b (2001).
145 Sudo, Y., Furutani, Y., Kandori, H. & Spudich, J. L. Functional Importance of the Interhelical Hydrogen Bond between Thr204 and Tyr174 of Sensory Rhodopsin II and Its Alteration during the Signaling Process. *J. Biol. Chem.* **281**, 34239-34245, doi:10.1074/jbc.M605907200 (2006).
146 Adams, P. D. *et al.* PHENIX: a comprehensive Python-based system for macromolecular structure solution. *Acta Crystallographica Section D: Biological Crystallography* **66**, 213-221, doi:10.1107/S0907444909052925 (2010).
147 Gushchin, I. *et al.* Active State of Sensory Rhodopsin II: Structural Determinants for Signal Transfer and Proton Pumping. *Journal of Molecular Biology* **412**, 591-600, doi:10.1016/j.jmb.2011.07.022 (2011).
148 Radzwill, N., Gerwert, K. & Steinhoff, H.-J. Time-Resolved Detection of Transient Movement of Helices F and G in Doubly Spin-Labeled Bacteriorhodopsin. *Biophysical Journal* **80**, 2856-2866, doi:10.1016/S0006-3495(01)76252-2 (2001).
149 Klare, J. P. *et al.* Probing the Proton Channel and the Retinal Binding Site of Natronobacterium pharaonis Sensory Rhodopsin II. *Biophysical Journal* **82**, 2156-2164, doi:10.1016/S0006-3495(02)75562-8 (2002).
150 Etzkorn, M. *et al.* Secondary Structure, Dynamics, and Topology of a Seven-Helix Receptor in Native Membranes, Studied by

Solid-State NMR Spectroscopy. *Angewandte Chemie International Edition* **46**, 459-462, doi:10.1002/anie.200602139 (2007).

151 Gordeliy, V. I. *et al.* Molecular basis of transmembrane signalling by sensory rhodopsin II–transducer complex. *Nature* **419**, 484, doi:10.1038/nature01109 (2002).

152 Dods, R. *et al.* From Macrocrystals to Microcrystals: A Strategy for Membrane Protein Serial Crystallography. *Structure* **25**, 1461-1468.e1462, doi:10.1016/j.str.2017.07.002 (2017).

153 Bordignon, E. *et al.* Structural analysis of a HAMP domain: the linker region of the phototransducer in complex with sensory rhodopsin II. *J Biol Chem* **280**, 38767-38775, doi:10.1074/jbc.M509391200 (2005).

154 Spudich, J. S. T. N. E. N. S. J. L. Constitutive activity in chimeras and deletions localize sensory rhodopsin II/HtrII signal relay to the membrane-inserted domain - Sasaki - 2007 - Molecular Microbiology - Wiley Online Library. doi:10.1111/j.1365-2958.2007.05983.x (2007).

155 Yoshida, H., Sudo, Y., Shimono, K., Iwamoto, M. & Kamo, N. Transient movement of helix F revealed by photo-induced inactivation by reaction of a bulky SH-reagent to cysteine-introduced pharaonis phoborhodopsin (sensory rhodopsin II). doi:10.1039/B315454H (2004).